

Contents

1 Theory	1
1.1 Optics	1
1.1.1 Fourier domain OCT	1
1.1.2 Optical imaging and information transfer	2
1.1.3 Relation between PSF, ESF and MTF	4
1.1.4 Confocal Laser scanning microscopy (CLSM)	4
1.2 Mechanics of fiber scanners	7
1.2.1 Piezoelectric tube actuators	7
1.2.2 Resonant Beam Theory	8
2 Design & Simulation	11
2.1 Design Requirements	11
2.2 Design overview	12
2.3 Optical Design of the OCT beam path	13
2.3.1 Fourier Plane Scanner	14
2.3.2 Component Selection	15
2.3.3 ZEMAX Simulation	16
2.3.4 Minimization of backreflections	17
2.3.5 Single Modality Probe	19
2.3.6 Simulated Optical Performance	19
2.4 Image acquisition: Spiral Scanning	19
2.4.1 Driving and Acquisition	21
2.5 Mechanical Design	22
2.5.1 Resonance frequency calculation	23
2.5.2 COMSOL simulation	23
3 Implementation	27
3.1 Polyimide Electrodes	28
3.1.1 Cleanroom processing	29
3.2 Fiber-GRIN Bonding	31
3.3 3D Printed Housing	31
3.4 Assembly	32
4 Experimental Characterization	35
4.1 Fiber Scanner Characterization	35
4.2 Dynamic behavior of the scanner	36

Contents

4.3	Laser Scanning Microscopy	36
4.3.1	Imaging	38
4.3.2	Lateral Resolution Measurement	39
4.3.3	Depth of Field Measurement	40
4.4	OCT Imaging	42

1 Theory

This work combines several principles of optics and mechanics to create an imaging device. Therefore, a review of some relevant theoretical fundamentals will ease the understanding of the design and functionality of the presented device.

Starting with the optical design, the probe uses the concept of Fourier Domain Optical Coherence Tomography (SD-OCT) to extract the depth information of the sample and the mechanism of Laser Scanning Microscopy (LSM) to acquire its lateral information. A LSM needs a scanning mechanism to displace laterally the focus position of an optical imaging device. In this work, this displacement is achieved by a tube shaped actuator which uses the piezoelectric effect to drive a thin resonant beam into resonance.

1.1 Optics

Optical coherence tomography (OCT) is a confocal, interferometric measurement method which allows the retrieval of depth information of a sample from its backscattered light. Due to its non-invasive nature, it is used in an expanding variety of medical imaging methods. Although there are extensive introductions to OCT, i.e. by Drexler and Fujimoto [1], this section briefly describes the underlying physical mechanism of OCT and confocal imaging.

1.1.1 Fourier domain OCT

The core functionality of OCT is implemented using a Michelson interferometer, as depicted in Figure 1.1.

In swept-source OCT (SS-OCT), a type of Fourier Domain OCT, the light source used in the interferometer originates from a narrowband laser with the ability to tune its wavenumber $k = \frac{2\pi}{\lambda}$ over a wide range. To gain intuition on how SS-OCT can extract depth information, consider a single reflector placed in the measurement arm at a distance z_{M1} . The intensity measured by the detector due to this mirror is described by the two beam interference equation

$$I_D(k) = I_{M1} + I_R + \sqrt{I_{M1} I_R} \cos(2k(z_{M1} - z_R)). \quad (1.1)$$

where I_{M1} and I_R are the light intensities reflected from the measurement and reference arm. If the distance between the sample reflector and the reference mirror $\Delta z = z_{M1} - z_R$ is zero or a multiple of π/k , the intensity at the detector will be at

1 Theory

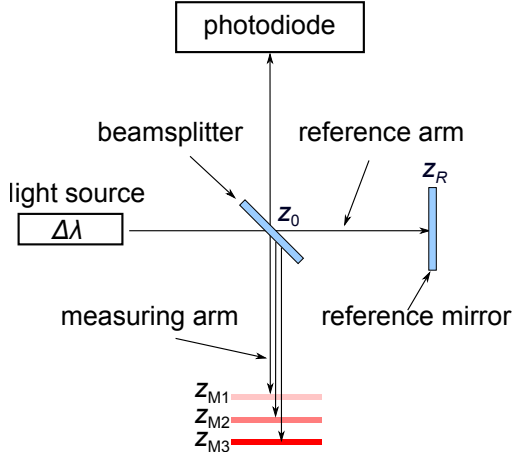


Figure 1.1: Schematic of a SS-OCT measurement system based on a Michelson interferometer, where the sample is modeled as a discrete number of reflectors at different depths and reflectivities. Modified with permission from [2]

maximum – for that particular wavenumber. If the laser source is swept across its tunable range, some wavenumbers will be interfere constructively in the detector, while others destructively, happening with a period in k of $\pi/\Delta z$. This relationship between wavenumber and intensity is named spectral interferogram, and encodes the reflector position.

The same analysis can be applied to multiple sample reflectors, each one of them contributing with a modulation of the spectral interferogram with a period of $\pi/\Delta z_i$. The resulting spectral interferogram, an example of which can be seen in Figure 1.2a for 3 reflectors, can be very complex, but after decomposing its harmonic component using a fourier transform, it unveils the position of the mirrors as cross-correlations and the distances between themselves as auto-correlations, as shown in Figure 1.2b. This last plot, showing the backreflected intensity vs z -position is usually named A-scan.

The ability of an SS-OCT system to resolve two reflective surfaces separated by a small z distance, termed *axial resolution* δz , improves with a wider wavenumber sweep range Δk , following

$$\delta z = \frac{2\sqrt{\ln(2)}}{\Delta k}. \quad (1.2)$$

The ability of the system to resolve two adjacent points, i.e. its *lateral resolution*, is independent of the axial resolution and completely determined by the optical system, as described in the next paragraphs.

1.1.2 Optical imaging and information transfer

OCT imaging uses a conventional optical system to illuminate and collect the backscattered photons from the sample. As such, it is affected by diffraction ef-

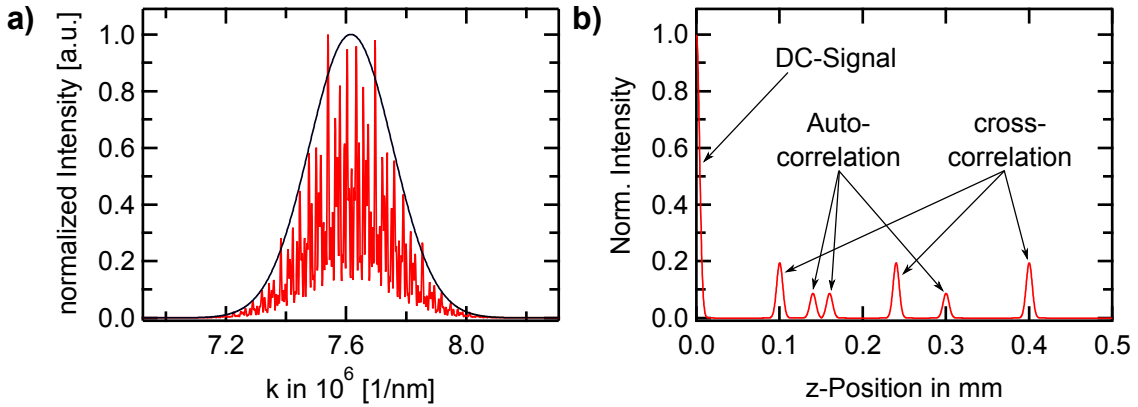


Figure 1.2: **a)** Spectral interferogram of a swept source laser with gaussian amplitude profile when used in OCT with no sample (blue) and with three discrete reflectors in the sample arm (red). **b)** A-scan calculated from the spectral interferogram in a) using the Fourier transform. Modified with permision from [2]

fects, which perform a spatial low-pass filtering of the object, limiting the imaging resolution.

Imaging in spatial domain: The PSF

To understand this phenomenon it is useful to resort to the concept of Point Spread Function (PSF). The PSF is the 3 dimensional image that a optical system creates from an infinitesimal object. Therefore, it can be considered as the impulse response of the system. As any object $f(x,y,z)$ can be described as a set of infinitesimally small points, its image can be computed as the convolution – or blurring – of each point of the object with the PSF of the optical system [3]:

$$b(x,y,z) = f(x,y,z) * PSF(x,y,z) \quad (1.3)$$

Imaging in frequency domain: The MTF

It is also possible to describe this blurring in spatial frequency domain. Here, the imaging process is modeled as a low-pass filtering of the frequency content of the object. If the object is described by its frequency content or spectrum $F(\mathbf{k})$ and the modulation transfer function $MTF(\mathbf{k})$ describes the optical filtering, the frequency content of the incoherent image can be calculated as

$$B(k_x, k_y, k_z) = F(k_x, k_y, k_z) \cdot MTF(k_x, k_y, k_z). \quad (1.4)$$

Notice that in the frequency domain, the spectrum of the object has to be simply multiplied by the MTF of the system, instead of convolved. Thus, working in the frequency domain eases the analysis of optical systems.

1 Theory

1.1.3 Relation between PSF, ESF and MTF

There is a fundamental mathematical relation between the MTF and the PSF: the MTF is the real part of the fourier transform of the PSF, i.e. the Optical Transfer Function (OTF) [3]:

$$OTF = \mathcal{F}(PSF) = MTF \exp(-iPTF). \quad (1.5)$$

This relationship is exemplified in Figure 1.3, where a PSF - MTF pair of a gaussian beam is shown.

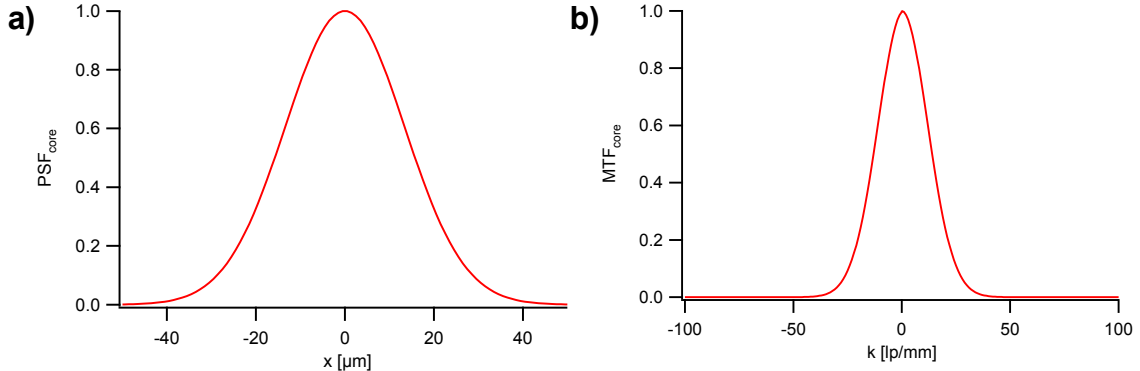


Figure 1.3: **a)** Simulated PSF of a gaussian beam focused by a lens. **b)** Corresponding MTF obtained through a fourier transform.

Measuring the PSF experimentally has the difficulty of requiring an "infinitesimally small" object to act as a *delta* function. To ease the process, it is possible to use an object with a *step* function, i.e. a sharp edge. The response of the system in this case is the convolution of the PSF with the *step* function

$$[\text{Step}(x)\mathbf{1}(y)] * \text{PSF}(x,y) = \text{ESF}(x) \quad (1.6)$$

and its result denominated Edge Spread Function ESF [3].

As the convolution with a *step* function is equivalent to integration, we find that

$$\int \text{PSF}(x)dx = \text{ESF}(x). \quad (1.7)$$

Thus, by simply differentiating the ESF it is possible to obtain the PSF, and by fourier tranform, the MTF of the system experimentally.

1.1.4 Confocal Laser scanning microscopy (CLSM)

The imaging topology used in this work is denominated Confocal Laser Scanning Microscopy (CLSM). This technique, represented in Figure 1.4, uses a fiber coupled laser source to project a focused beam in the sample. Some of the backscattered light from the sample is collected back to the fiber and detected by a photodiode. By scanning the focus position through the sample it is possible to obtain 2D or 3D images.

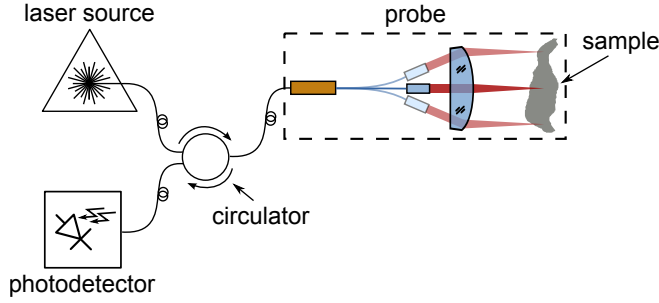


Figure 1.4

Modeling of CLSM

To understand the optical modeling of a CLSM we begin considering the probe as an illumination device, i.e. a projector. In this case, laser light coming from the optical fiber will be focused by the optical system in a plane located at its working distance. The focused spot won't be infinitesimally small due to two reasons: first, as in any optical system, diffraction takes place and blurs it with its $PSF_{\text{optics}}(\mathbf{r})$, defined by the NA and the wavelength of the focused beam. Furthermore, the gaussian intensity distribution at the core of the fiber has a certain extent, characterized by its Mode Field Diameter (MFD). Once projected in the image plane, the MFD will be magnified by the optical system by a factor of $1/M$, where M is the magnification of the beam defined as $f_{\text{fiber}}/f_{\text{objective}}$. This gaussian spot can be conceptually considered as the PSF due to the extended core of a fiber PSF_{core} .

Thus, the projected spot, whose distribution is determined by the extended source of the fiber and the magnification and diffraction of the optical system, can be considered as the illumination PSF, calculated by convolution as

$$PSF_{\text{ill}}(\mathbf{r}) = PSF_{\text{core}}(\mathbf{r}M) * PSF_{\text{optics}}(\mathbf{r}) \quad (1.8)$$

or equivalently, the illumination MTF

$$MTF_{\text{ill}}(\mathbf{k}) = MTF_{\text{core}}(\mathbf{k}/M) \cdot MTF_{\text{optics}}(\mathbf{k}) \quad (1.9)$$

following the PSF-MTF relationship. This behavior can be observed in Figure 1.5a, where MTF_{core} and MTF_{optics} are simulated according to the design values of this work.

The next step in the description of the CLSM considers the detection or collection of the backscattered light. If all the light coming from the fiber is projected in the PSF_{ill} , we can use the Helmholtz reciprocity property of light to state that the photons originating within this PSF will be collected by the fiber and detected by the photodiode. Thus, the detection PSF is equivalent to the illumination PSF,

$$PSF_{\text{det}}(\mathbf{r}) = PSF_{\text{ill}}(\mathbf{r}) = PSF_{\text{core}}(\mathbf{r}M) * PSF_{\text{optics}}(\mathbf{r}) \quad (1.10)$$

or equivalently,

$$MTF_{\text{det}}(\mathbf{k}) = MTF_{\text{ill}}(\mathbf{k}) = MTF_{\text{core}}(\mathbf{k}/M) \cdot MTF_{\text{optics}}(\mathbf{k}) \quad (1.11)$$

1 Theory

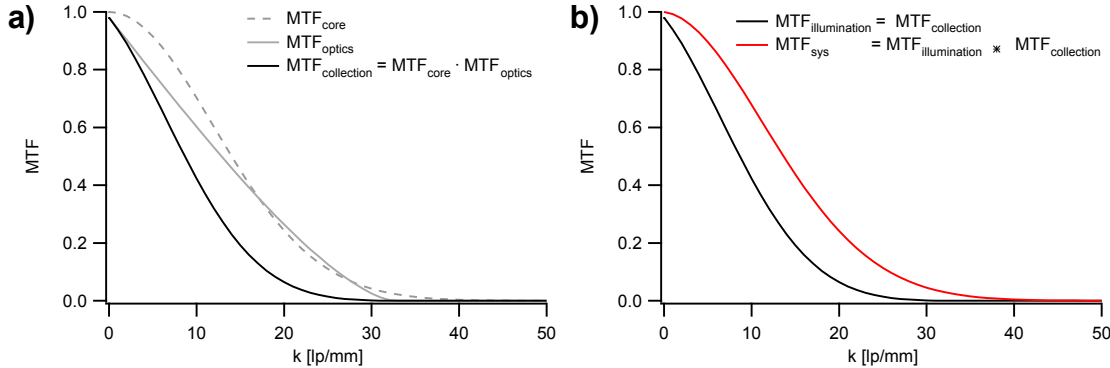


Figure 1.5: **a)** Simulated MTF of the illumination or collection of a single point using the proposed optical system. The collection MTF is limited by the finite size of the fiber core and the diffraction of the optical system. **b)** MTF of the imaging system, calculated as the convolution of illumination and detection MTFs.

Considering now the complete imaging process of a confocal laser scanning microscope, a photon traveling through the fiber is projected inside the PSF_{ill} , with a higher probability of illuminating the focus position. After being scattered by the sample, it has a high probability of being collected by the detector, as it is also in the center of the PSF_{det} . It can be concluded that both PSFs are multiplied together, and thus the complete imaging system PSF given by

$$PSF_{\text{sys}}(\mathbf{r}) = PSF_{\text{ill}}(\mathbf{r}) \cdot PSF_{\text{det}}(\mathbf{r}) \simeq PSF_{\text{det}}(\mathbf{r})^2 \quad (1.12)$$

or equivalently, using the autoconvolution - squaring equivalence between spatial and frequency domain

$$MTF_{\text{sys}}(\mathbf{k}) = MTF_{\text{ill}}(\mathbf{k}) * MTF_{\text{det}}(\mathbf{k}) \simeq AC[MTF_{\text{det}}(\mathbf{k})]. \quad (1.13)$$

These operations are numerically calculated in Figure 1.5b.

Finally, the resultant image can be calculated following Equation 1.3:

$$b(\mathbf{r}) = f(x',y',z') * PSF_{\text{sys}}(x',y',z'). \quad (1.14)$$

Resolution of CLSM

A final word regarding the resolution of CLSM: the autoconvolution of the PSF which characterizes CLSM can lead to an increase in resolution compared with conventional microscopy *if the system is diffraction limited*. That implies using an illumination source and an detection aperture with pinholes significantly smaller than the diffraction limited PSF in these surfaces, so that PSF_{core} becomes a delta function and $PSF_{\text{ill}}(\mathbf{r}) = PSF_{\text{optics}}(\mathbf{r})$.

In this work, the pinhole is defined by the diameter of the GRIN lens, which truncates the collimated beam at its $1/e^2$ level, corresponding with a truncation factor $k = 1$. This limits the resolution of the system compared with a fully confocal system, as seen in 1.6.

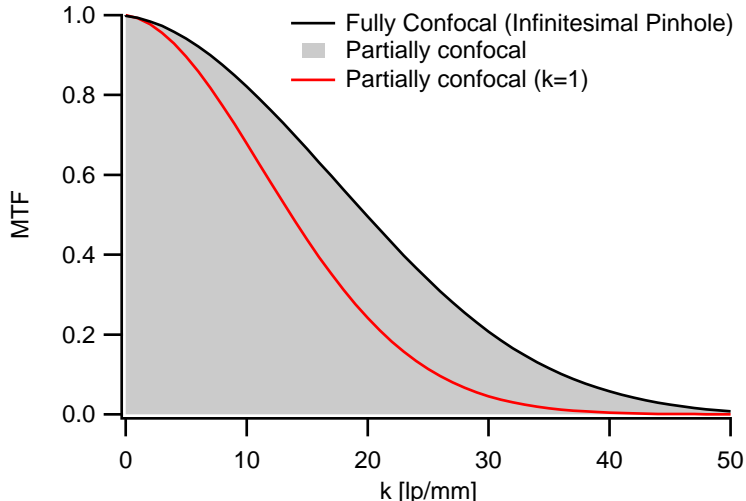


Figure 1.6: Comparison of the simulated MTF of a confocal system with infinitesimally small pinhole (black) and with a pinhole with a truncation factor k equal to 1 ($D = D_{\text{beam},1/e^2}$), red. The shaded area represents the possible MTFs for any truncation factor.

1.2 Mechanics of fiber scanners

The previous section focused in the acquisition of the depth information of a single column of a sample. But, in order to acquire a full, 3D volume of the sample, a 2D scanning mechanism is required. This section briefly goes over the physics and fundamental aspects of piezoelectric tube fiber scanners, starting with their actuation mechanism followed by the analytical modeling of their resonant scanning fiber.

1.2.1 Piezoelectric tube actuators

A piezoelectric tube is a solid state actuator consisting of a tube made of radially polarized piezoelectric material with inner and outer electrodes, as depicted in Figure 1.7a. The outer metallization of the tube is divided in four quarter electrodes, which generate a radial electric field in the sandwiched portion of the piezoelectric material, shown in Figure 1.7b. If a voltage difference is applied to two opposite electrodes of the tube, one side will contract while the other will expand due to the piezoelectric effect. This behavior is modeled [4] linearly by $\epsilon = d_{31}E$, where ϵ represents the in-plane strain, d_{31} the piezoelectric strain coefficient, and E the out-of-plane electric field magnitude. This asymmetry creates a bending moment across the axis of the tube, inducing its deformation. If one end of the actuator is kept static, the tip of the actuator will deflect and tilt according to the applied voltage. A 2D scanner can be created out of this setup if two independent signal control the horizontal and vertical electrodes, as shown in Figure 1.7c.

1 Theory

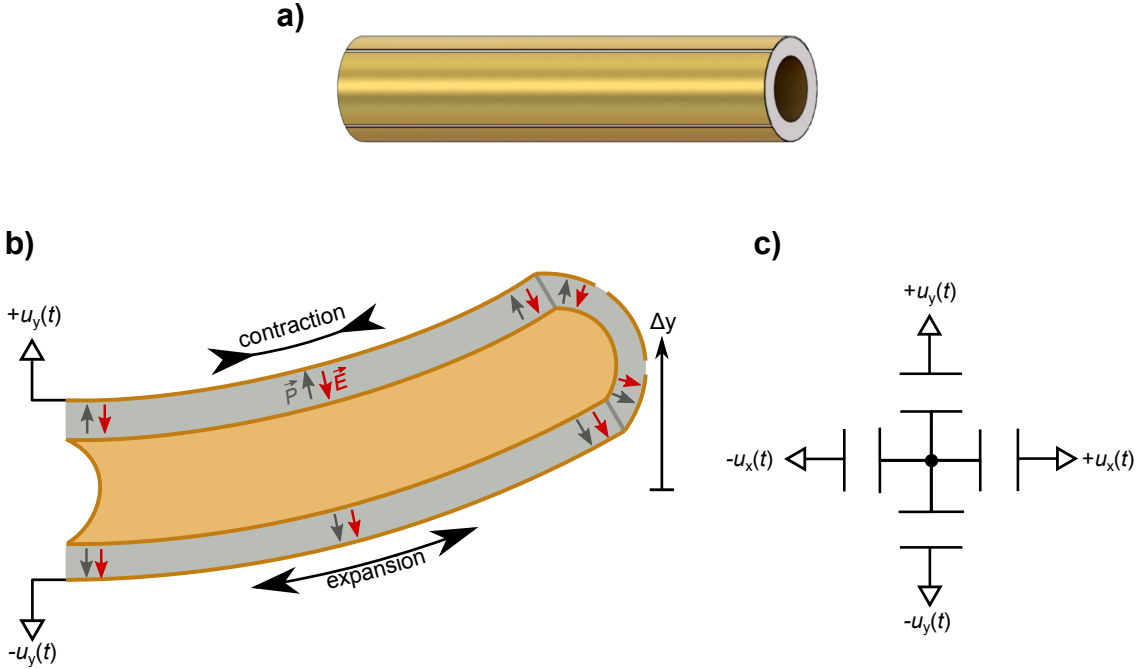


Figure 1.7: **a)** Render of a piezoelectric tube. **b)** Half-cut drawing of a piezoelectric tube in actuated state. The radial polarization of the piezoelectric material is shown in gray arrows. A voltage $\pm u_y(t)$ is applied to the top and bottom outer electrodes, creating a radial electric field under those electrodes, depicted as red arrows. Due to the piezoelectric effect, the top of the tube contracts, while the bottom expands, inducing a bending of the tube. **c)** Electrical model of the piezoelectric tube with four electrodes.

The deflection of the tip of the tube is linear with the applied voltage, and in case of bipolar operation, estimated by [5] to be

$$\Delta y = V \frac{2\sqrt{2}d_{31}L^2}{\pi Dh}$$

, where V is the applied voltage to each opposing electrode, d_{31} is the piezoelectric strain coefficient of the material in direction perpendicular to the polarization direction, L is the length of the tube, D its outer diameter and h the thickness of its wall. Thus, longer tubes with a thinner diameter and wall thickness maximize the deflection of the tip. Typical deflections for small actuators lie in the order of 20 nm/V.

1.2.2 Resonant Beam Theory

The piezoelectric actuator described in the last paragraphs couples mechanical energy into the cantilever of the scanner, formed by a fiber optic segment to which a

GRIN lens is glued, as depicted in Figure 2.12a. As the scanner uses mechanical resonance to amplify the small displacements of the actuator, it is important to model the resonance frequency of such a system.

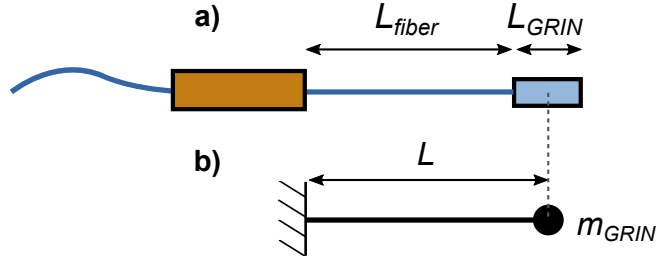


Figure 1.8: **a)** Drawing of the piezoelectric scanner: piezoelectric tube, fiber and GRIN lens. **b)** Simplified mechanical diagram obtained by modeling the fiber as a weightless cantilever and the GRIN lens as a point mass.

The fiber-GRIN assembly can be modeled as a point-loaded, fixed-free cantilever and the GRIN lens weight can be concentrated in its center of gravity, as represented in Figure 2.12)b).

Now, by applying the ideal mass-spring harmonic resonator equation, the resonance frequency can be estimated as

$$f_{\text{res}} = \frac{1}{2\pi} \sqrt{\frac{K_{\text{cantilever}}}{m_{\text{GRIN}}}} \quad (1.15)$$

where $K_{\text{cantilever}}$ represents the elastic constant of the fiber cantilever. Considering it as a fixed-free, point loaded cantilever, its spring constant can be calculated as

$$K_{\text{cantilever}} = \frac{3EI}{L^3} = \frac{3\pi}{4} \frac{E_{\text{fiber}} r_{\text{fiber}}^4}{L^3} \quad (1.16)$$

following the Euler-Bernoulli theory [6] and considering that the moment of inertia of the cylindrical fiber is given by $I_{\text{fiber}} = \frac{\pi}{4} r^4$.

1 Theory

2 Design & Simulation

The aim of this work is to design and test a miniaturized OCT microscope as a component of a multi-modal endoscopic probe. This probe consists of two spectrally-separated optical paths that run partially in parallel through a micro-optical bench. This approach allows independent design of the optical parameters of the two imaging modalities – such as the numerical aperture (NA) or depth of field – while still providing a geometrical overlap of the two acquired images. An integrated tubular piezoelectric fiber scanner is used to perform en face scanning required for three dimensional OCT measurements. This scanning engine has an outer diameter of 0.9 mm and a length of 9 mm, and features custom fabricated 10 μm thick polyimide flexible interconnect lines to address the four piezoelectric electrodes.

The following section describes the conception and design of the endoscope, starting from the medical and geometrical requirements, through analytical modeling and towards the optimization of each component.

2.1 Design Requirements

The OCT microscope should fulfill the following requirements:

Mechanical Requirements

- The scanner, electrical connections and optics should fit in a channel with a $1 \text{ mm} \times 1 \text{ mm}$ cross section located in the lower level of a multimodal bench. This way the total cross section of the endoscope can be kept below $3 \times 2 \text{ mm}^2$.
- Its length should be minimized to allow its integration in flexible-head endoscopes.
- The field of view should be maximized for a 2 mm diameter objective lens, that is shared with the endomicroscopy beam path.
- The scanning speed should be adequate for the sampling rates characteristic of SD-OCT ($\sim 100 \text{ kHz}$).

Optical Requirements

- The microscopy and OCT imaging fields should be coaxial to avoid parallax errors.

2 Design & Simulation

- The OCT field should be telecentric to avoid field curvature distortions.
- The lateral resolution and depth of field should be adequate for OCT i.e. with numerical aperture ranging from 0.02 to 0.05.
- The backreflections inside the probe should be minimized to reduce any loss of contrast and penetration depth.

2.2 Design overview

The main challenge of this work is to design an OCT scanning mechanism compact enough to be placed in a thin, buried channel of a multimodal probe. Although it is theoretically possible to keep a scanner at the proximal end of the endoscope and use a coherent fiber bundle as a relay, there are inherent drawbacks of this method when applied for OCT, such as low light throughput, cross-talk and mechanical rigidity [7].

Another challenging requirement is the superposition of the images acquired by the different modalities. If the optical axes are not coaxial, the fields will be shifted and tilted due to parallax error — which gains importance at the small working distances common in endoscopy.

To overcome these problems, and taking into account the above-mentioned requirements, we propose a design based on the HYAZINT multimodal probe [?]. By creating a two layer microbench, it is possible to bury the OCT resonant fiber scanner in the bottom level and merge both modalities in the top level using a dichroic beamsplitter. A schematic of this mechanism can be seen in Figure 2.1.

The base of the microbench with dimensions of $13 \times 2 \times 1 \text{ mm}^3$ is realized by standard silicon bulk micromachining. On the top layer, the bench accommodates the full field imaging optics that consists of a dichroic beamsplitter cube with dimensions of $2 \times 2 \times 2 \text{ mm}^3$ to separate the two beam paths and two plano-convex lenses with 2 mm diameter, which form a full field microscope. To achieve a highly compact opto-mechanical design, the components of the OCT beam path are buried within a cavity in the base of the micro bench. On the bottom layer a gradient index lens (GRIN lens) with a diameter of $350 \mu\text{m}$ is directly glued to the tip of a $80 \mu\text{m}$ single mode fiber to collimate the infrared light of the OCT system with a center wavelength of $\lambda_o = 1311 \text{ nm}$. A spiral scanning of the OCT beam path is achieved by an angular scanner implemented using a piezoelectric tube actuator.

This actuator, called resonant fiber scanner, is able to scan a collimated beam by more than $\pm 5^\circ$ by mechanically amplifying the subtle vibration of a piezoelectric actuator. An objective lens focuses the beam on the tissue and transforms the angular displacement into a translation. By driving the scanner in two axes with two sinusoids at different phases, it is possible to sample a 2D area of the object in a spiral fashion [8], as explained in detail in Section 2.3.

The rest of this chapter shows the design and development of the OCT imaging path for the multi-modal probe. However, in order to independently test the be-

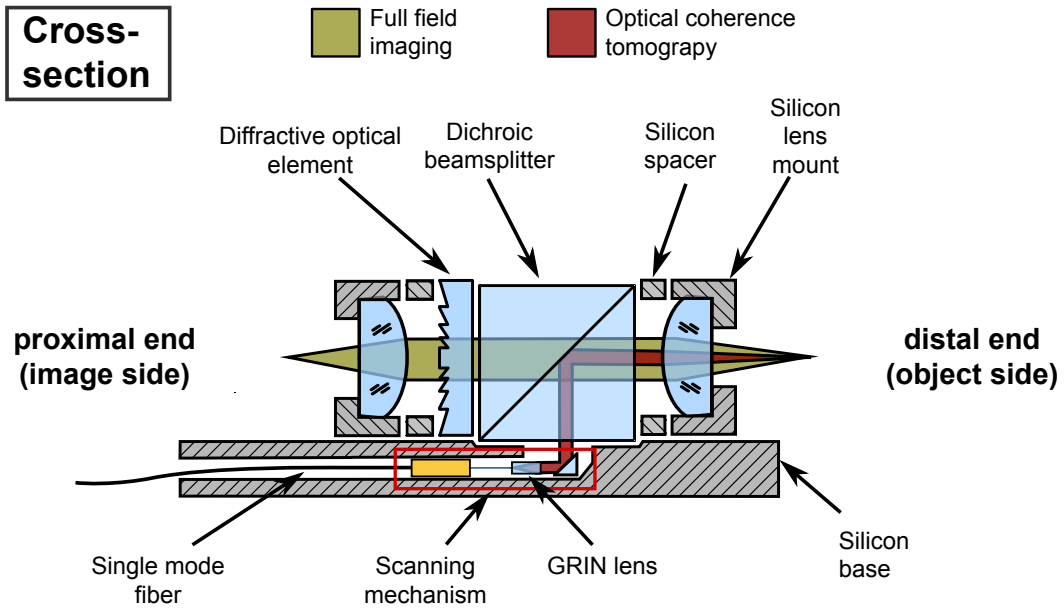


Figure 2.1: Schematic of the MEMS endomicroscope based on the HYAZINT probe [?]. Two glass lenses glued directly to the dichroic beamsplitter cube form the full field microscopy beam path. A silicon aperture is used to reduce the spherical aberrations. Buried beneath the full field optics, a single mode fiber glued to a collimating GRIN lens forms the OCT channel. The single-mode fiber is centered in a piezoelectric tube to create a fiber scanner enabling 3D OCT. A reflecting micro-prism glued to a dichroic beamsplitter cube combines the two beam paths.

havior of the OCT scanner and optics, a single modality probe was fabricated as a demonstrator. Both systems are mechanically and optically equivalent – the only difference is the presence of the beam splitter. For completeness, both multi-mode and single-mode optical systems are described.

2.3 Optical Design of the OCT beam path

This section explains in detail the design of the OCT optics and its scanning mechanism. Starting with the concept of a Fourier plane scanner, the most relevant design equations are derived, which guide the selection of the optical components to achieve the desired performance, eventually verified by optical simulation.

2.3.1 Fourier Plane Scanner

The OCT beam path is designed as an distal-side telecentric system to avoid distortions in the 3D OCT measurement. To achieve this, the fiber scanner is driven with small angles and is positioned such that the lateral and angular movement of the scanner imitates the beam angles that can be observed in the collimated region of a classical telecentric lens system. Figure 2.2 illustrates this approach. The whole scanner is buried in a channel with a inner diameter of 1 mm limiting the movement of the scanner to a maximum angle θ of 5° that allows a maximum FOV of 1 mm of the OCT beam path.

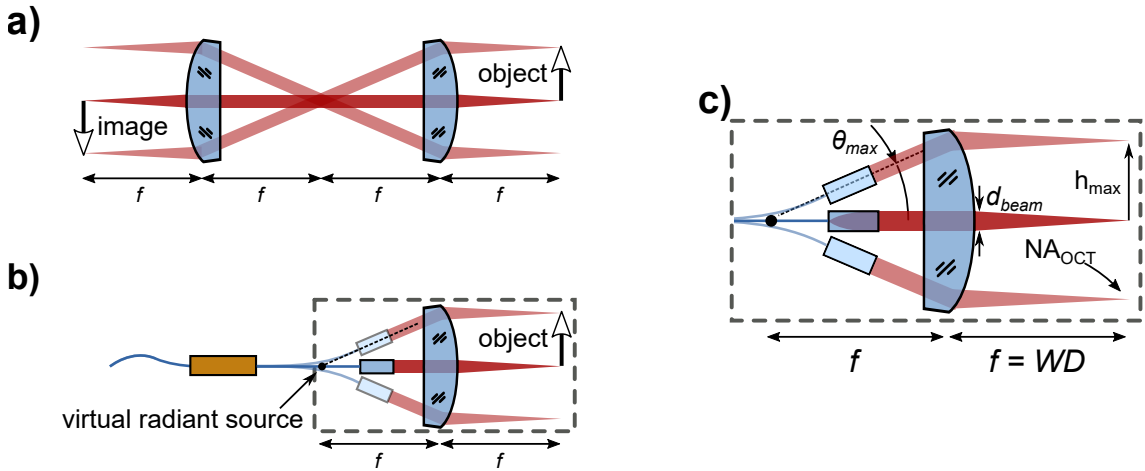


Figure 2.2: a) Illustration of a classical telecentric system. The height of the object is translated into an angle θ in the collimated region between the two lenses. This angle is again translated into a corresponding image height by the second lens. b) Illustration of the OCT beam path using a fiber scanner in first resonance mode without micro prism and BS. The movement of the GRIN lens due to the fiber scanner and the distance between the GRIN lens and the focusing lens creating the same optical behavior as it can be observed in a classical distal-sided telecentric system. c) Nomenclature used in this work.

For the scanner to work as a Fourier plane scanner, at any point of the oscillation the output beam from the GRIN lens should point to a fixed virtual radiant source. This is fulfilled if the bending shape of the scanner is linear with the amplitude and thus, the ratio of the GRIN lens angle to its vertical displacement is kept constant $y = d \cdot \tan \theta \simeq d \cdot \theta \Rightarrow \frac{\theta}{y} = const$ (refer to Figure 2.3).

In a Fourier plane scanner, the numerical apertures and focal lengths of the scanning and objective lens are related by the diameter of the beam in the intermediate region between both lenses. Thus, based on the schematic of Figure 2.2c, the following geometrical optics relations are obtained: $d_{beam} \simeq 2 \cdot f_{GRIN} \cdot NA_{fiber}$ and $d_{beam} \simeq 2 \cdot f_{obj} \cdot NA_{OCT}$. By combining them together,

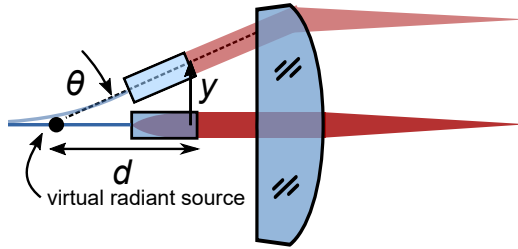


Figure 2.3: Schematic of the Fourier plane scanner at rest and at an arbitrary angle θ . If the scanner behaves linearly, the output beam will appear to come from a fixed virtual radiant source regardless of the scanning amplitude.

$$f_{\text{GRIN}} \cdot \text{NA}_{\text{fiber}} = f_{\text{obj}} \cdot \text{NA}_{\text{OCT}} \quad (2.1)$$

the main design equation for the scanner is obtained. Note that these equations use a small angle approximation valid for small NA: $\tan[\sin^{-1}(\text{NA})] \simeq \text{NA}$. In this case, as any NA is smaller than 0.25, the error of this simplification is smaller than 2%.

2.3.2 Component Selection

The design equations that were obtained in the previous section relate all the optical components together. Therefore, once the desired NA is chosen, there is only a free variable available. In this case, the major constraint is given by the commercial availability of the single mode fiber, so the selection of the rest of the components will follow from it.

The only commercially available single mode fiber working in our wavelength range and with thinned cladding diameter (refer to Section 2.5) is *Thorlabs SM980G80*, with a diameter of 80 μm and with $\text{NA}_{\text{fiber}} = 0.18$ at $\lambda = 1.33 \mu\text{m}$.

In order to collimate the output from the fiber without clipping the gaussian beam, a GRIN lens with an NA_{GRIN} higher than NA_{fiber} is needed. A good fit from the GRINTECH catalog is *GT-LFRL-035-024-20-CC (1550)*, with an $\text{NA}_{\text{GRIN}} = 0.20$ and $f_{\text{GRIN}} = 0.91 \text{ mm}$.

Now, by using the relation in Equation 2.1 we can design $f_{\text{objective}}$ by choosing an adequate NA_{OCT} . To preserve a high depth of field (DOF), allow enough space for the beamsplitter and a long working distance, a narrow NA_{OCT} is preferred – in the range of 0.020 - 0.025. By choosing an intermediate NA_{OCT} of 0.022, the focal length of the objective lens

$$f_{\text{obj}} = f_{\text{GRIN}} \frac{\text{NA}_{\text{fiber}}}{\text{NA}_{\text{OCT}}} = 0.91 \text{ mm} \frac{0.18}{0.022} = 7.5 \text{ mm} \quad (2.2)$$

can be selected. The manufacturing of this lens was performed by *Optik+* with a plano-convex spherical geometry, as one of the facets of the lens has to be cemented to the beamsplitter cube.

2 Design & Simulation

The field of view (FOV) of the OCT modality can be now calculated considering the maximum angular deflection of the GRIN lens in the tip of the scanning fiber by

$$h_{\max} = f_{\text{obj}} \cdot \tan \theta_{\max} = 7.5 \text{ mm} \cdot \tan 5^\circ = 0.66 \text{ mm}, \quad (2.3)$$

equivalent to a FOV of 1.2 mm for a θ_{\max} of $\pm 5^\circ$, as calculated in section 2.5.

2.3.3 ZEMAX Simulation

Once the components are selected, it is possible to validate the theoretical analysis of the optical design by performing a raytracing simulation. Using ZEMAX, the fiber facet is modeled as the waist of a gaussian beam source, the GRIN lens is modeled using a design file from the manufacturer and the prism, beamsplitter and planoconvex lens are modeled geometrically according to the provided mechanical drawings. The result is shown in Figure 2.4.

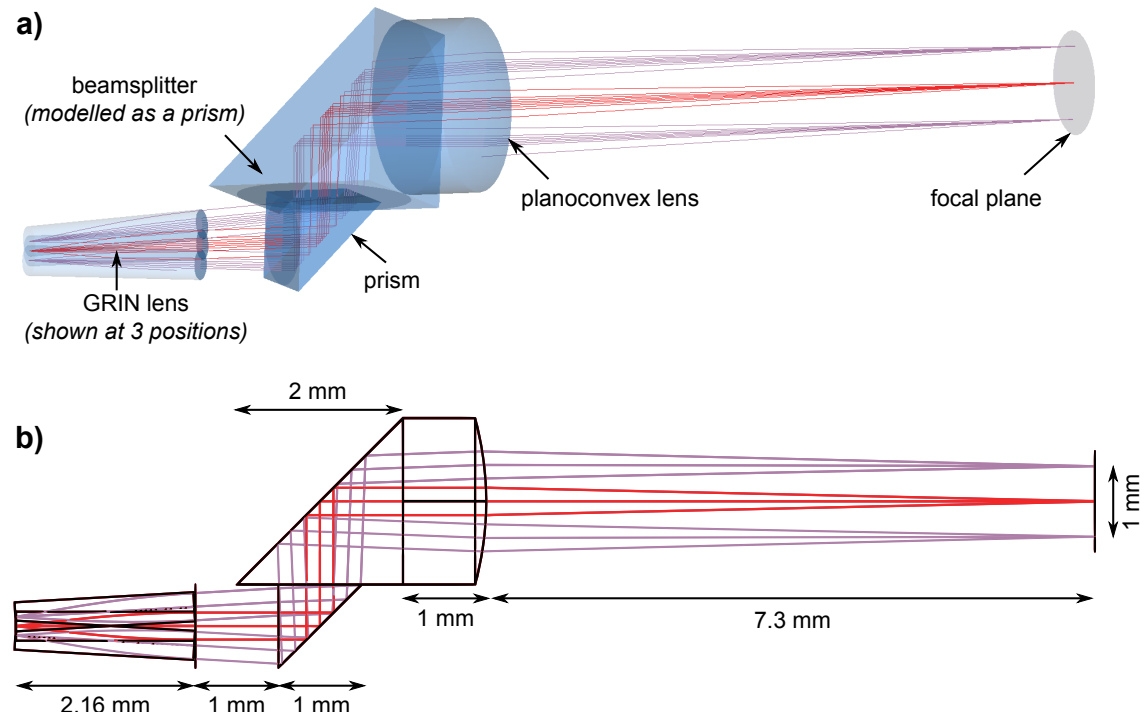


Figure 2.4: **a)** 3D ZEMAX raytracing of the OCT beam path for the center (red rays) and marginal (purple rays) position of the GRIN lens. Note that as the OCT beam path is reflected in the hypotenuse of the beamsplitter, it can be modeled as a 45° prism. **b)** Cross section of a) showing the most relevant dimensions.

The three overlapping rectangles on the left simulate the rest position (red) and maximum deflection (purple) of the GRIN lens. The gap between GRIN lens and

2.3 Optical Design of the OCT beam path

prism is calculated so that the focus of the planoconvex lens coincides with the virtual radiant source of the scanner.

Due to the low NA_{OCT} and the good optical quality of the GRIN and planoconvex lenses, the aberrations in this design are negligible and thus has an optical performance close to the diffraction limit. Figure 2.5 proves this behavior by comparing the MTF (Modulation Transfer Function) of an ideal optical system with the simulated MTF of the system which is described.

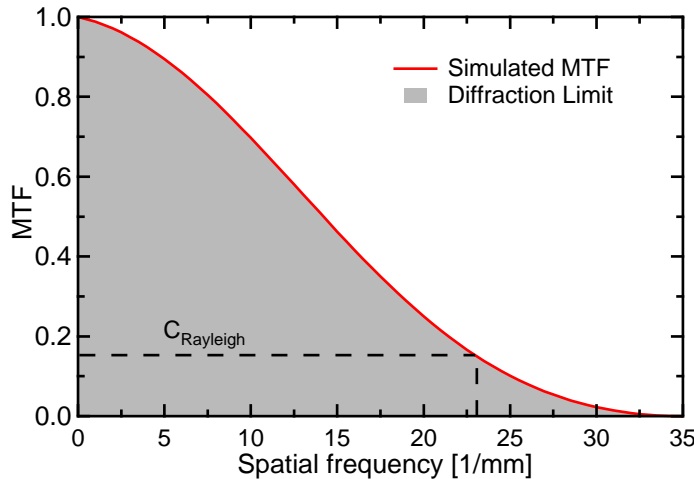


Figure 2.5: Simulated MTF curve of the OCT beam path for the bimodal probe. It can be seen that the system is diffraction limited and provides a lateral resolution of 23.3 lp/mm or 43 μm .

2.3.4 Minimization of backreflections

In OCT, any backreflection inside the probe increases the background intensity at the spectrometer, thus limiting its dynamic range. The consequences are higher noise, lower penetration depth and lower contrast of the resultant image. Therefore any source of backreflections in the design should be carefully considered and minimized. The main ones are marked in Figure 2.6 and explained in the following list:

1. **Fiber - GRIN interface:** Starting from the proximal side, the facet of the fiber and the GRIN lens are two parallel glass surfaces separated by a small gap. Although the beam is not collimated in this region, a small portion of light can be coupled back to the fiber. In order to minimize any backreflections, fiber and GRIN are glued together using a refractive-index-matched optical adhesive (*NOA 76*, from *Norland Products*). This way there is no glass to air interface and the maximum refractive index step is reduced to 0.05.

2 Design & Simulation

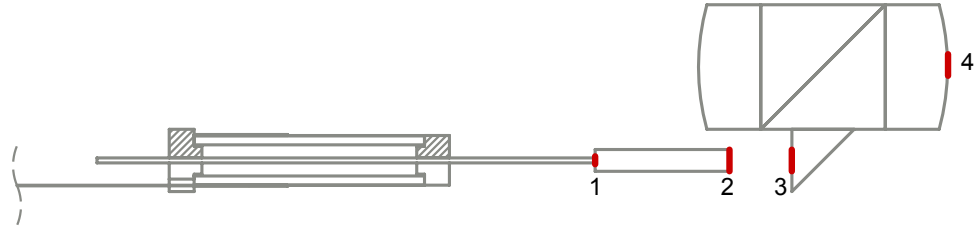


Figure 2.6: Schematic of the multimodal probe showing the main interfaces where backreflections can originate inside the probe (red). 1) Fiber - GRIN. 2) GRIN - air gap. 3) Air gap - prism. 4) Objective - air.

2. **GRIN - gap interface:** The next interface is the distal facet of the GRIN lens. This is a critical backreflection source – regardless of the scanning angle, there is normal, collimated light incidence. To avoid this problem without resorting to delicate and expensive antireflection coatings, the GRIN lens is manufactured with a 1° tilt exit facet. According to geometrical optics, this tilt induces a vertical shift in the position of the backreflected focal point $\Delta y = f \tan(2\alpha)$ which in this system equates to $0.91 \text{ mm} \cdot \tan(2^\circ) = 31 \mu\text{m}$.

The result is visible in the simulation from Figure 2.7: the backreflected light is focused back $31 \mu\text{m}$ away, effectively missing the core of the fiber – which has a diameter smaller than $5 \mu\text{m}$.

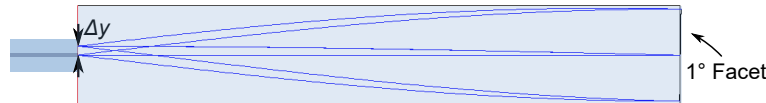


Figure 2.7: Schematic showing the raytracing simulation of a beam exiting from the distal facet of the fiber and being coupled into a GRIN lens with a tilted exit facet. Thanks to it, the backreflected light misses the core of the fiber and is thus not coupled back to the OCT system.

3. **Air - prism interface:** Due to collimated incidence, this interface can produce important backreflections, but only in the resting position of the GRIN lens, when the free end of the GRIN lens is pointing perpendicular to the surface of the prism. To minimize reflections in this situation it is possible to resort to anti-reflection coatings in the facet of the prism.
4. **Objective lens - air interface:** After the prism, the beamsplitter and objective lens are cemented together, making any backreflections negligible. The objective lens has an interface with air, but has an anti-reflection coating on this surface. Furthermore, due to the curved surface of this lens, the backreflected light won't be focused back in the single mode fiber significantly.

2.3.5 Single Modality Probe

As stated in the Design Overview, in order to independently test the behavior of the OCT scanner and optics, a single modality probe was fabricated as a demonstrator. Its optical design, depicted in Figure 2.8, emulates the multimodal design from Figure 2.4 by unfolding its optical path. The main difference is the lack of the prism and beamsplitter and the orientation of the planoconvex lens, which is flipped to reduce the backreflections caused by normal incidence on the planar side of the lens.

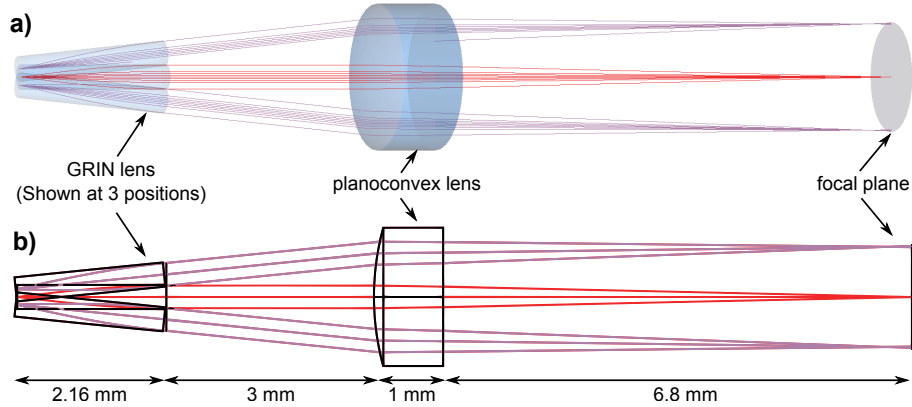


Figure 2.8: a) 3D ZEMAX raytracing of the OCT beam path for the center (red rays) and marginal (purple rays) position of the GRIN lens in the single modality demonstrator. b) Cross section of a).

The equivalence of both systems is emphasized by the similarity of their simulated MTF. Again, Figure 2.9 indicates that the single modality demonstrator is diffraction-limited.

Due to these similarities, it is expected that any experimental result obtained with the demonstrator can be easily transferred to the behavior of the bimodal probe.

2.3.6 Simulated Optical Performance

To conclude the *Design and Simulation* chapter, the most important characteristics of the components of the OCT microscope are listed in Table 2.1 and the simulated performance in Table 2.2.

2.4 Image acquisition: Spiral Scanning

As described in the previous section, the OCT optical setup samples the object at only a single point. Thus, the focus point has to be 2D-scanned over the surface of the sample to obtain 3D OCT images.

A very compact solution to achieve this are resonant fiber scanners. These devices use the concept of mechanical resonance to amplify 300-fold the subtle movement

2 Design & Simulation

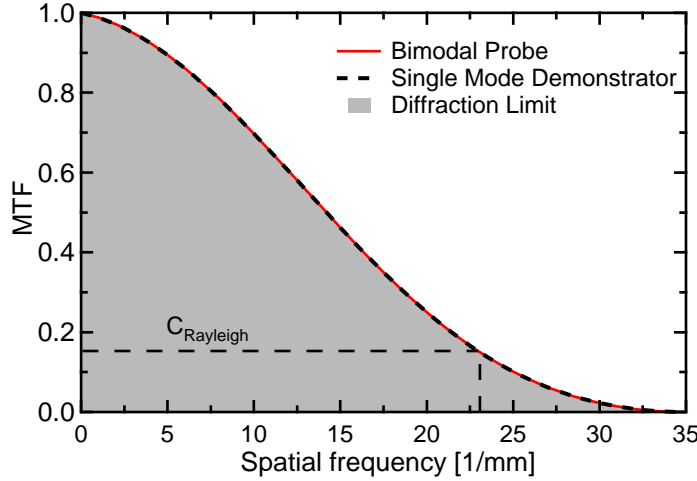


Figure 2.9: Simulated MTF curve of the OCT beam path for the bimodal probe and the single modality demonstrator. It can be seen that both implementations are optically equivalent and diffraction limited, providing a lateral resolution of 23.3 lp/mm or 43 μm .

Table 2.1: Summary of the most relevant characteristics of the optical components used in the OCT modality.

Parameter	Value
Single mode fiber NA	0.18
GRIN lens NA	0.2
GRIN lens focal length	0.91 mm
Planoconvex lens focal length	7.5 mm

Table 2.2: Simulated optical performance and characteristics of the OCT modality. All resolution values follow the Rayleigh convention of 15.5% modulation [2].

Parameter	Bimodal Probe	Single Mode Demonstrator
Distal Side NA	0.022	0.022
Working Distance	7.3 mm	6.8 mm
Field of View	1.2 mm	1.5 mm
Depth of Field	3.4 mm	3.4 mm
Lateral Resolution	43 μm	43 μm

of a piezoelectric actuator into a big displacement and angular deflection of the tip of a scanning fiber.

As any resonant system, the movement of the scanning fiber is constrained to

harmonic oscillations within a frequency close to its resonance frequency f_{res} . This requirement constraints the possible scanning patterns to harmonic movements at f_{res} , excluding then raster scanning, which require at least an axis working out of resonance. Then, conventional alternatives are Lissajous [9] and spiral scanning. In order to ease the reconstruction of the image, this work implements the latter.

The following pages describe the concept of spiral scanning, its characteristics, limitations and implementation.

2.4.1 Driving and Acquisition

The piezoelectric tube which drives the scanner has four outer gold electrodes to control the lateral movement of the scanner, as described in ???. Two independent voltage sources control the vertical and horizontal movement of the actuator by addressing the corresponding pair of electrodes. If sine and cosine signals of the same frequency f_{drive} are used to drive the scanner, the GRIN lens will oscillate in a circle of constant radius. If now the amplitude of these signals is modulated with another signal of frequency f_{mod} , the resultant trajectory will be spiral, as illustrated in Figure 2.10.

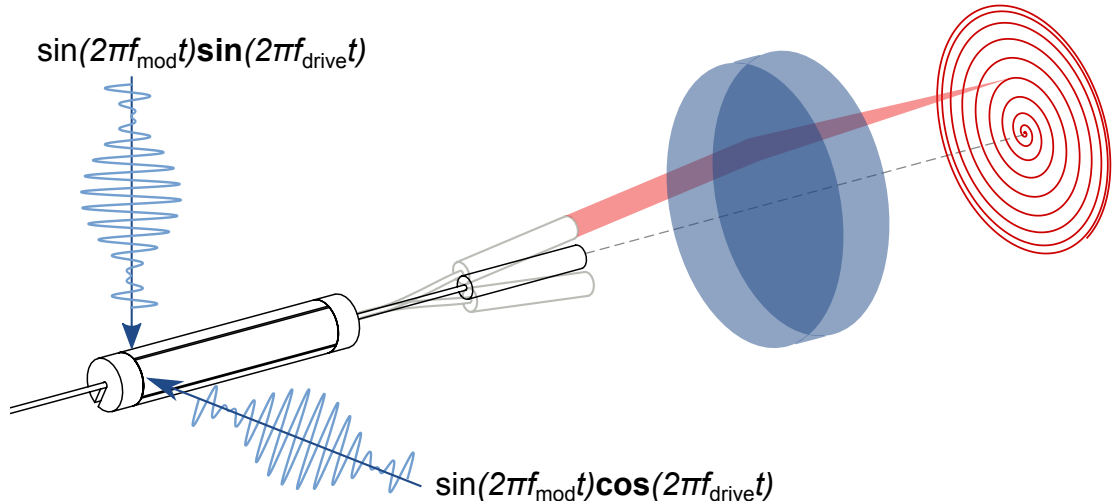


Figure 2.10: Schematic of the piezoelectric tube, fiber, GRIN and objective lens focusing the OCT beam (red) in a plane. The piezoelectric tube is driven with two independent amplitude modulated sine and cosine signals to generate a spiral pattern, used to acquire an image.

During the full period of the spiral pattern $T_{\text{spiral}} = f_{\text{mod}}^{-1}$, two complete frames are acquired, one while the spiral grows, another while it shrinks. The whole pattern can be divided in $N_{\text{rings}} = f_{\text{drive}}/f_{\text{mod}}$ individual rings, as depicted in Figure 2.11, each one acquired in a period $T_{\text{ring}} = f_{\text{drive}}^{-1}$. Thus the number of sample points that can be acquired in an individual ring

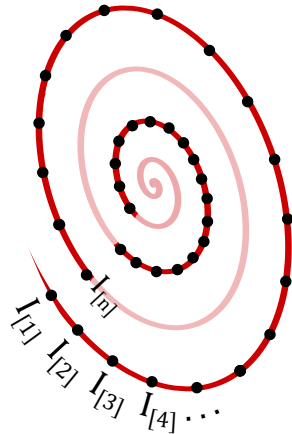


Figure 2.11: Section of a spiral trajectory highlighting two different rings. The n black dots represent the sampling points of each ring. Notice that in the inner ring the sampling density is higher than in the outer one.

$$n = \frac{f_s}{f_{\text{drive}}} \quad (2.4)$$

depends only on the driving frequency of the scanner f_{drive} and the sampling frequency f_s of the spectrometer, which is usually constant. This value is very important, as it defines the spatial sampling density.

In order to fulfill the Nyquist theorem, the spacing between two adjacent sample points should be smaller than the Airy radius of the laser spot, . This condition is easily fulfilled in the inner rings of the spiral, as there the focus spot has a small speed, but as the radius of the spiral grows, so does the scanning speed and therefore the distance between sample points, as seen in Figure 2.11.

It is clear then that spiral scanning shows a non-uniform sampling distribution across the imaging field. Thus, to avoid undersampling in the outer areas, the number of samples per ring n should be as high as possible. As OCT systems have a relatively small sampling frequency (~ 100 kHz), the resonant frequency needs to be below 1 kHz to achieve more than 100 acquired points per ring of the spiral.

2.5 Mechanical Design

As explained in the previous section, in any resonant system, its geometrical and mechanical characteristics fully define the operating frequency range, and with it, constrain the way the final image can be sampled.

In the following paragraphs the behavior of the fiber scanner is mechanically modeled, and this information used to choose the most relevant fabrication parameters leading to an adequate resonant frequency for OCT.

2.5.1 Resonance frequency calculation

The scanner used in the probe consists of a piezoelectric tube which drives a beam composed of a single mode fiber and a GRIN lens into resonance, as depicted in Figure 2.12a.

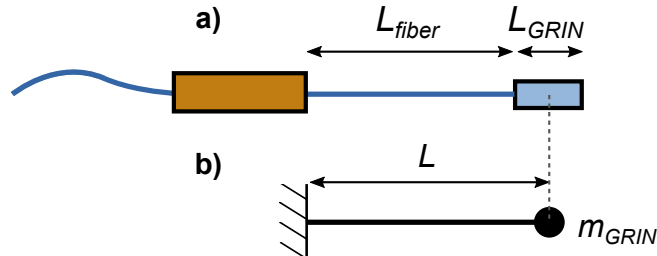


Figure 2.12: a) Drawing of the piezoelectric scanner: piezoelectric tube, fiber and GRIN lens. b) Simplified mechanical diagram obtained by modeling the fiber as a weightless cantilever and the GRIN lens as a point mass.

The Euler-Bernoulli method can be used to estimate the resonant frequency of this scanner as detailed in subsection 1.2.2. The resulting equations 1.16 and 1.15 show how the different mechanical properties of the scanner influence its resonant frequency. Thus, this frequency can be reduced in different ways: increasing the cantilever length L , decreasing the radius of the fiber r_{fiber} or increasing the mass at the tip m_{GRIN} . First, by having a GRIN lens attached at the tip, the resonance frequency is reduced by a factor of 62%. Furthermore, by choosing a fiber with 80 μm instead of the standard 125 μm , the resonance frequency can be lowered by an extra factor of 60%, as the sensitivity of the resonance frequency to the diameter of the fiber is quadratic. Under these conditions, the resonant frequency vs. length of the cantilever formed by a 80 μm fused silica fiber with the chosen GRIN lens is computed in Figure 2.13 using Equations 1.16 and 1.15.

In order to select the length of the scanner there are two things to consider. As the scanner is buried in a 1 mm channel, the maximum displacement of the GRIN lens is limited to $\pm 325 \mu\text{m}$. Within that small displacement we want to achieve the maximum angular deflection of the GRIN lens to maximize the FOV, what can be achieved by using shorter fiber lengths. This shows a trade-off with the density of sampling N_T , which is increased with longer fiber lengths. To balance those terms, we chose a a total scanner length of 4.5 mm, which fulfills all the before-mentioned requirements, as Table 2.3 shows.

2.5.2 COMSOL simulation

In order to validate the theoretical analysis of the previous section, a multiphysics finite element analysis was performed using *COMSOL*. For that matter, the actuator was modeled as a radially polarized piezoelectric material (*PIC 151*) and the rest of the structure as fused silica. The excitation voltage is a sinusoidal symmetrical

2 Design & Simulation

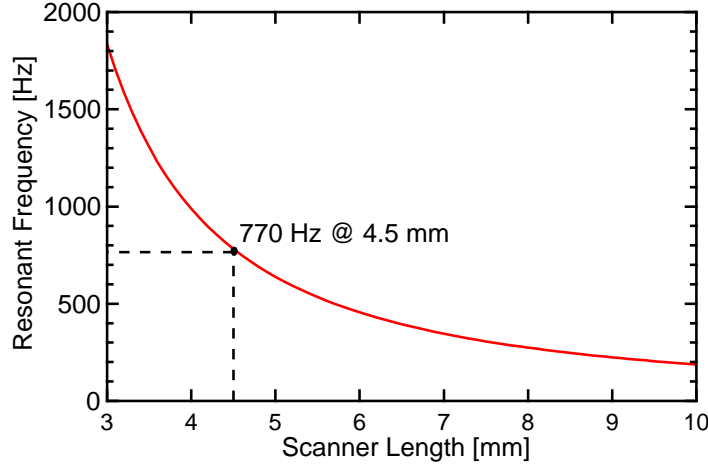


Figure 2.13: Resonant frequency of the scanner as a function of the total scanning tip length ($L_{\text{fiber}} + L_{\text{GRIN}}$). The chosen working point is labeled in the plot.

Table 2.3: Mechanical characteristics of the fiber scanner at its designed working point.

Cantilever length	4.5 mm
Resonant Frequency	770 Hz
Max. angular deflection	5°

potential between the top and bottom electrodes of the tube. Note that, as the system undergoes small deflections, it is simulated assuming linear behavior [10] without incurring in important deviations.

As the first step, the resonant frequency of the system is simulated. An Eigenfrequency study calculates the first mode resonance at 762 Hz, which closely matches the analytical estimation of 770 Hz. The mode shape at resonance is shown in Figure 2.14, where it can be observed that the actuator and the base of the fiber are almost static, confirming the resonant behavior of the scanner.

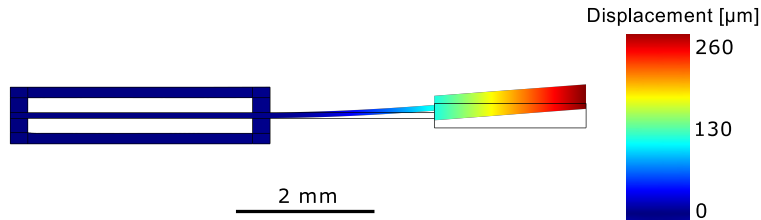


Figure 2.14: COMSOL simulation showing a cross section of the scanner maximum deflection at resonance. The deformed structure is color coded showing the total displacement from the rest position (shown outlined).

Thanks to the multiphysics simulation, it is also possible to check the electric field distribution inside the piezoelectric tube. As can be seen in Figure 2.15, for a symmetrical actuation in the top and bottom electrodes with a voltage of ± 75 V, most of the volume under these electrodes experiences a field magnitude close to the expected theoretical value $E = U/d = 75 \text{ V}/150 \mu\text{m} = 500 \text{ V/m}$, which is under the safe operating field of *PIC 151*, ranging from $+1000 \text{ V/m}$ to -700 V/m . Only some fringe areas exceed these values, which could become depolarized with time.

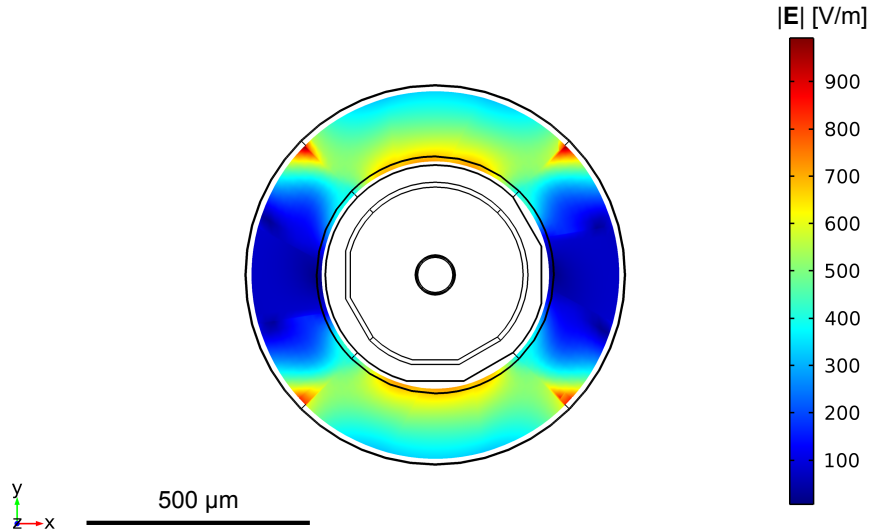


Figure 2.15: Magnitude of the electrical field inside a cross-section of the piezoelectric tube with an excitation voltage of ± 75 V applied to the top and bottom electrodes.

2 Design & Simulation

3 Implementation

This chapter details the implementation of the probe shown in Figure 3.1, which serves as a demonstrator of the fiber scanner design and evaluation tool of the optical performance of the OCT beam path.

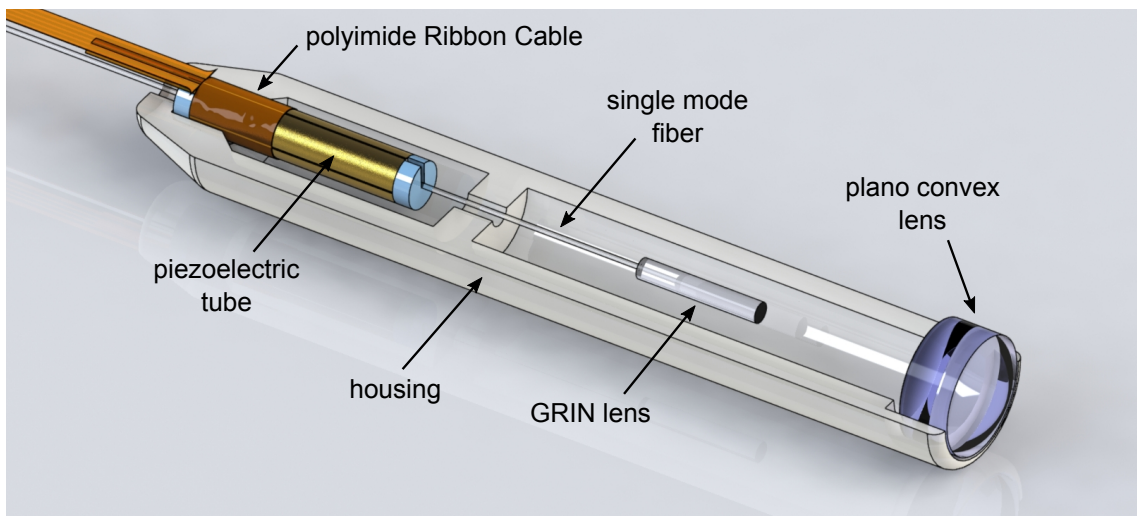


Figure 3.1: CAD of the single modality demonstrator with the top of the housing removed. Total length: 9 mm.

The design can be summarized as follows: The piezoelectric actuator has four outer gold electrodes to control the lateral movement of the scanner. The addressing of these electrodes is realized by a ribbon cable, which is wrapped around the piezoelectric tube. The single mode fiber is centered in the piezoelectric tube and the GRIN lens bonded to the tip of this fiber. This arrangement enables a compact fiber scanner with a total length of 9 mm and a resonance frequency of 750 Hz optimized for an OCT system with an A-Scan repetition rate of 100 kHz.

The following paragraphs describe the manufacturing process and assembly of the most relevant components of the probe, beginning with the fabrication of the polyimide electrodes used for contacting the piezoelectric tube and proceeding with details of the necessary assembly steps to fabricate the scanner, leading to the assembly of the complete probe.

3.1 Polyimide Electrodes

The first challenge that appears in the manufacturing of the scanner lies in contacting the four external electrodes of the piezoelectric tube.

Due to the small diameter of the tube (800 µm), creating a reliable interface between the driving circuit and its electrodes is not trivial. Other piezosscanner implementations use soft soldering and insulated copper wires [11], [12], [13], but the soldering process can damage the piezoelectric material, as it is exposed to temperatures above its Curie temperature. This method also increases the diameter of the actuator significantly, as a solder blob is needed.

Instead, this design uses a polyimide ribbon cable which is wrapped around the piezotube and addresses its four external electrodes using vias. Its geometry, cross section and application over the tube is depicted in Figure 3.2, while Figure 3.3 shows its complete design.

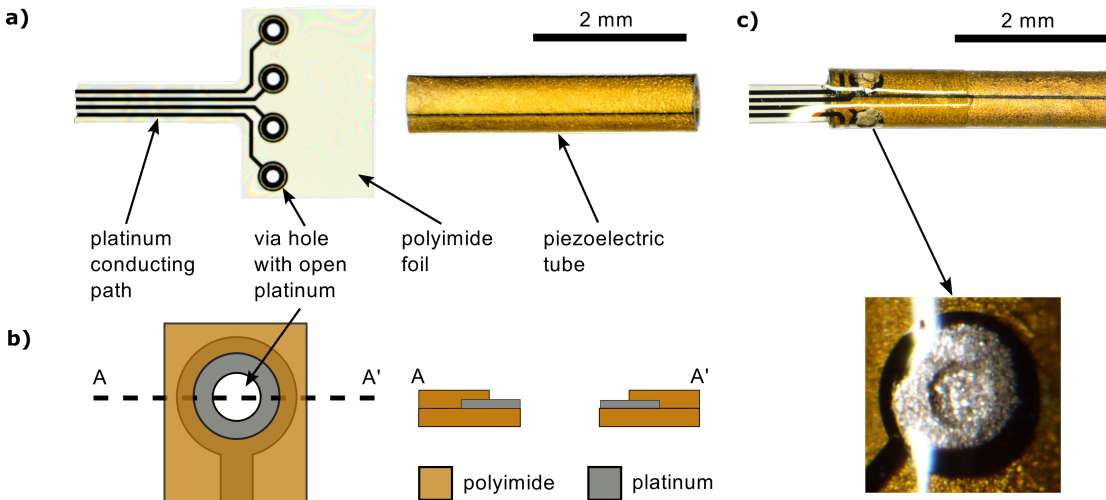


Figure 3.2: Polyimide electrode design. **a)** *Left:* Photo of the polyimide ribbon cable with four vias to contact the four gold electrodes of the piezoelectric tube. *Right:* Piezoelectric tube. **b)** Schematic of one via and its cross section. The platinum around the via is partly uncovered to improve the electrical connection between the cable and the piezoelctric tube. **c)** Photography of a polyimide ribbon cable, wrapped around the piezoelectric tube that is electrical connected through the vias by conductive glue. **d)** Microphotograph of the via after bonding with conductive glue.

It is manufactured using a cleanroom process similar to the one used for cuff electrodes for nerve stimulation [14] and consists of platinum tracks and via holes embedded in a polyimide substrate. One end the cable is shaped to fit a zero insertion force (ZIF) connector. The other end can be rolled around the piezoelectric tube, allowing the bonding to its gold electrodes using conductive glue (Araldite 2020 with 80% wt. silver particles).



Figure 3.3: Render of a manufactured polyimide electrode. The left side fits a ZIF connector, the right side is rolled around the piezoelectric tube to address its electrodes.

3.1.1 Cleanroom processing

The polyimide ribbon cables are manufactured and singulated at wafer level. The process involves spin coating a $5\text{ }\mu\text{m}$ layer of polyimide, over which 100 nm of platinum is sputtered and then patterned by liftoff, defining the conductive traces. On top of it, a second $5\text{ }\mu\text{m}$ layer is spincoated. Finally, the vias, openings and external shape are patterned through reactive ion etching (RIE). This process is described in Figure 3.4 and the resultant wafer in Figure 3.5.

3 Implementation

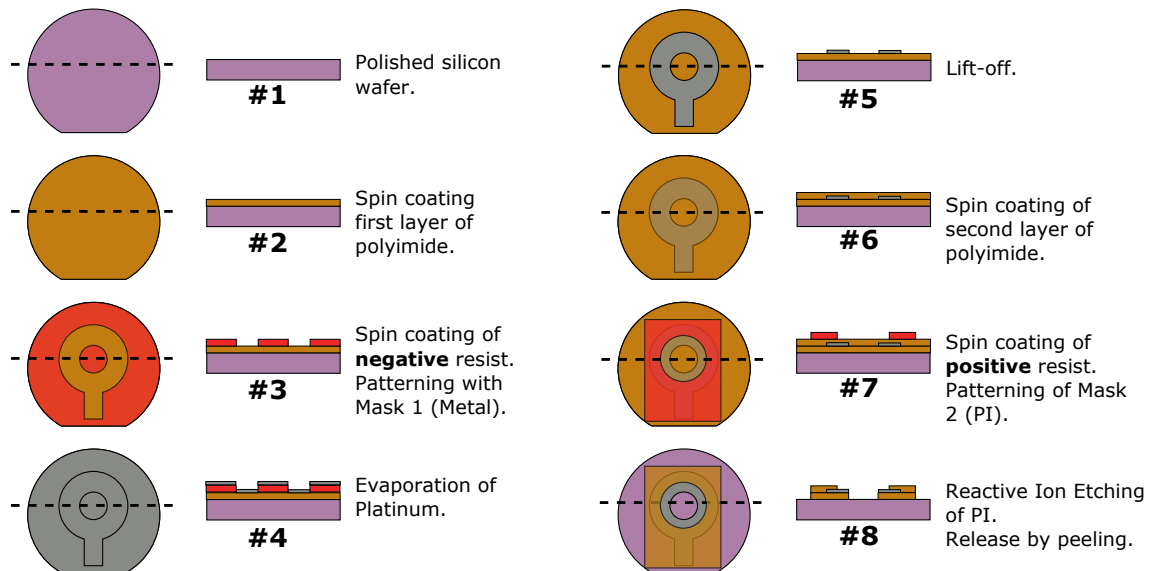


Figure 3.4: Illustration of the fabrication of a polyimide-platinum via. The first column shows the top view of the wafer, while the cross section is depicted in the second column.

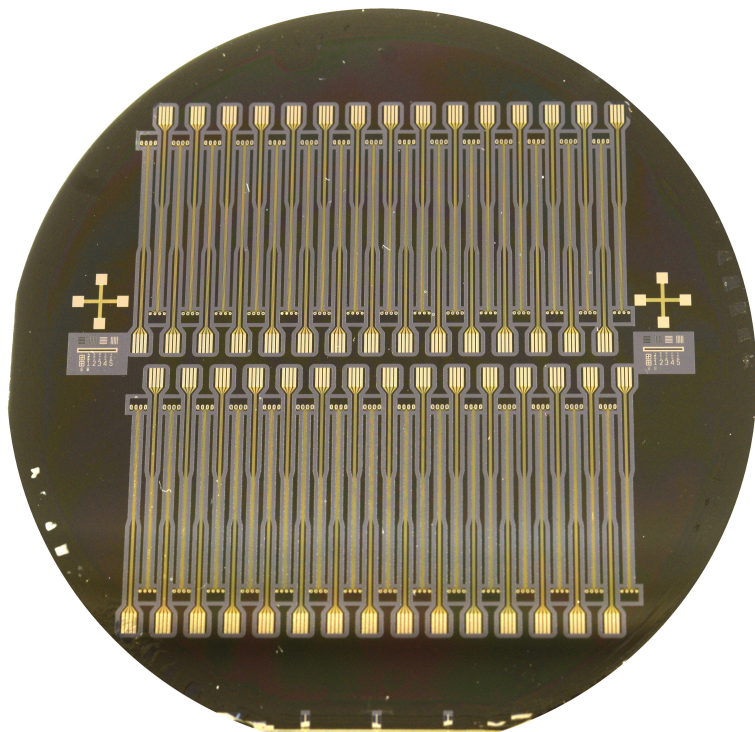


Figure 3.5: True scale photography of a 100 mm wafer containing 60 polyimide electrodes.

3.2 Fiber-GRIN Bonding

Another step that has to be performed before the final assembly of the probe is to bond the GRIN lens to the end of the fiber optically and mechanically. This interface is critical: first, because it is subjected to very high forces due to the oscillation of the scanner, and second, because any angular or displacement error would degrade the optical quality.

To overcome these challenges, fiber and GRIN lens are aligned together using a custom made, KOH-etched silicon alignment tool. The geometry of the KOH-etched grooves together with the cylindrical shape of both components allow the precise angle and position control of the fiber and GRIN lens. Once in place, a drop of index-matched UV-curable glue (NOA 76) bonds the components together. The wetting behavior and surface tension of the glue create a symmetrical wedge which provides extra mechanical integrity, as can be seen in Figure 3.6.

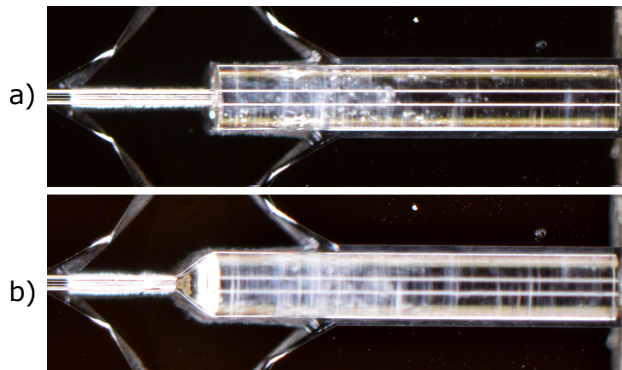


Figure 3.6: **a)** Photography of the tip of the fiber (right) and GRIN lens (left) seating in the alignment tool. **b)** Bonding with UV-curable adhesive.

3.3 3D Printed Housing

The bimodal probe is designed to be assembled using the silicon bench technology [2]. But for the demonstrator, a process with reduced complexity, which allows faster design adjustments has been tested: using a 3D printed polymer structure for both assembly and housing.

This is possible because, even though the dimensional accuracy of the printed housing is lower than its silicon counterpart, the optical components of the demonstrator allow relatively high placement tolerances, as the beam is collimated in the region between GRIN lens and objective lens. This way, simple alignment structures which are 3D-printed within the housing allow the proper placement of all components, as shown in Figure 3.7. The main dimensions of the housing are depicted in Figure 3.8.

The housing is manufactured using a *B9Creator* stereolithography printer, which allows the polymerization of an acrylic resin with a lateral resolution of 30 µm.

3 Implementation

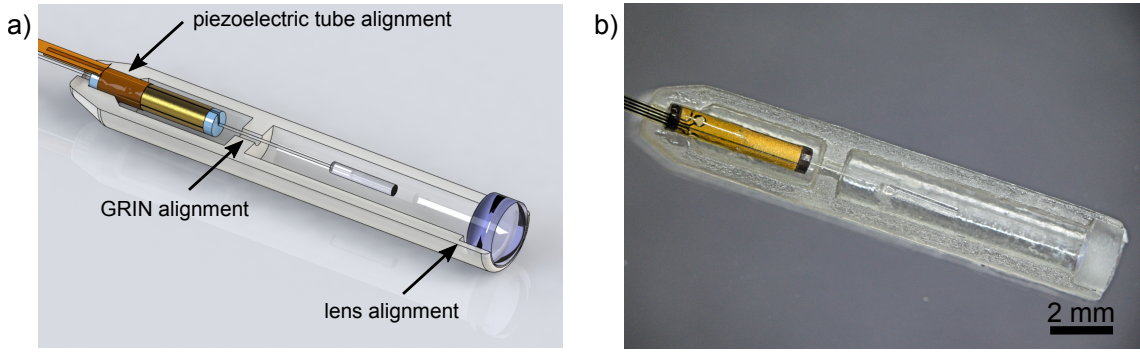


Figure 3.7: CAD (a) and photography (b) of the single modality probe with alignment features.

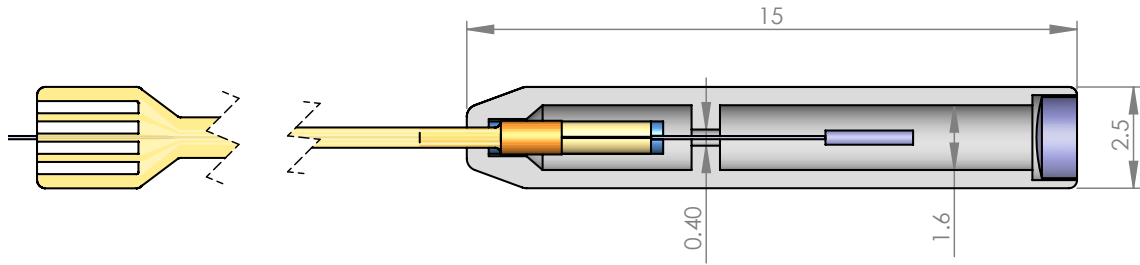


Figure 3.8: Top view of the single modality probe showing the main dimensions of the housing.

3.4 Assembly

Once all the components are ready, the assembly is performed by hand using the multiple alignment features of the housing. The exploded view in Figure 3.9 shows the placement of the components prior to assembly, followed by the final encapsulation. This process is summarized as follows:

1. The GRIN lens is bonded to the end of the fiber using the alignment tool (section 3.2).
2. The GRIN-fiber assembly is slid through the piezotube and centered with FR-2 fittings, which are glued to the piezotube using cyanocrylate.
3. The piezotube-fiber-GRIN assembly is placed in the housing and glued in place using cyanocrylate with help of the alignment structures.
4. The planoconvex lens is placed in the bottom half of the housing and glued using UV-curable optical glue.
5. The probe is closed with the top half of the housing and sealed with UV-curable glue.

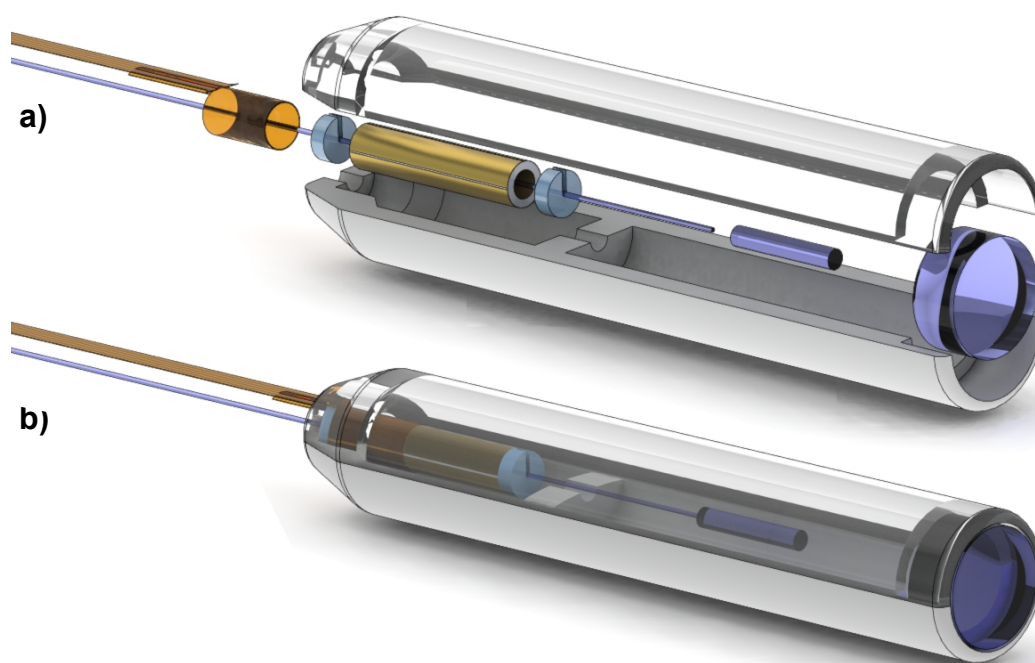


Figure 3.9: **a)** Exploded view of the components which form the single modality probe. **b)** Render of the complete probe after assembly.

3 Implementation

4 Experimental Characterization

The following pages describe the performance of the OCT scanner demonstrator probe. First, the optomechanical characteristics of three manufactured probes are compared with their expected values. Later, a set of driving parameters optimized for each probe is used to image a sample using spiral scanning. The challenges and solutions associated with this method are discussed, highlighting the different data processing methods. Eventually, OCT measurements of biological samples are presented.

4.1 Fiber Scanner Characterization

Three single modality demonstrator probes were assembled to test the repeatability of the process. For each probe, a characterization step was performed in order to measure its resonance frequency, laser coupling efficiency, backreflectivity and maximum unobstructed field of view. These results are summarized in Table 4.1.

Table 4.1: Optomechanical characteristics of three assembled single modality probes compared with their expected values, calculated for a cantilever length of 4.5 mm.

	Design Value	Probe 1	Probe 2	Probe 3
Cantilever Length [mm]	4.5	4.45	4.44	4.10
Field of View [mm]	1.3	1.1	1.2	1.2
Resonant Frequency [Hz]	762	744	765	842
Coupling Efficiency	-	0.53	0.61	0.58
Backreflectivity [%]	-	0.011	0.04	0.018

- **Cantilever Length:** The cantilever length which was varied between 4.10 mm and 4.45 mm to test the behavior of the scanner under different parameters.
- **Field of View:** At a certain scanning amplitude, the laser beam becomes shadowed by the edges of the optical components. In the case of the single modality probe, this happens due to the walls of the housing, which by design limit the FoV to 1.3 mm. Any misalignment between the optical axis of the scanner and the symmetry axis of the housing further reduces the FoV due to decentering.

4 Experimental Characterization

- **Resonant Frequency:** The resonance frequency was measured by driving the scanner with a sweeping sinusoidal signal and observing the amplitude of oscillation. The variability of the cantilever length explains the change of the resonant frequency: shorter cantilevers exhibit lower resonance frequency, as their stiffness is higher. It can be seen that for Probes 1 and 2, whose cantilever length is close to the designed 4.5 mm, their resonant frequency is within 3% of the expected 762 Hz.
- **Coupling Efficiency:** This value was calculated by measuring the intensity of the beam exiting the probe divided by the power of the light source at its output fiber connector. Thus, it includes the losses from the FPC fiber connector, fiber interfaces and backreflections. It is believed that the main source of loss is the connector, which has variable losses up to 30%, depending on the quality of the polishing of the fiber facet and any surface imperfection or contamination.
- **Backreflectivity:** In order to measure the backreflected light intensity it is necessary to send and receive light through the scanning fiber. To achieve this, is it possible to reuse a FD-OCT measurement setup with some modifications. As seen in Figure 4.1, broadband infrared light with a center wavelength of $\lambda_o = 1311$ nm and a bandwidth of $\Delta\lambda = 90$ nm from an SLED is coupled to a circulator, which forwards it to the probe. Any light which is backreflected inside the probe, together with backscattered light from the sample is coupled back to the fiber and forwarded by the circulator to the photodetector. In case that the probe is pointing to free space, only light backreflected from the optical components is measured. By dividing this intensity by the source intensity and taking into account the coupling efficiency of the system, the backreflectivity was measured to be well controlled under 0.02%. The variability within probes can be attributed to differences in alignment and gluing of the fiber and GRIN lens.

4.2 Dynamic behavior of the scanner

4.3 Laser Scanning Microscopy

This section explains how it is possible to use the single modality probe as a laser scanning microscope (LSM) and use the acquired images to assess its lateral resolution and depth of field. As LSM and OCT modalities use the same wavelength, these results are also representative for OCT imaging.

Once that a suitable set of driving parameters has been found for each probe, and the scanner is performing an spiral pattern, the first step to assess the system performance is to couple light into the probe and measure the intensity of light which is backreflected from the sample. Then, by knowing the backreflected intensity at

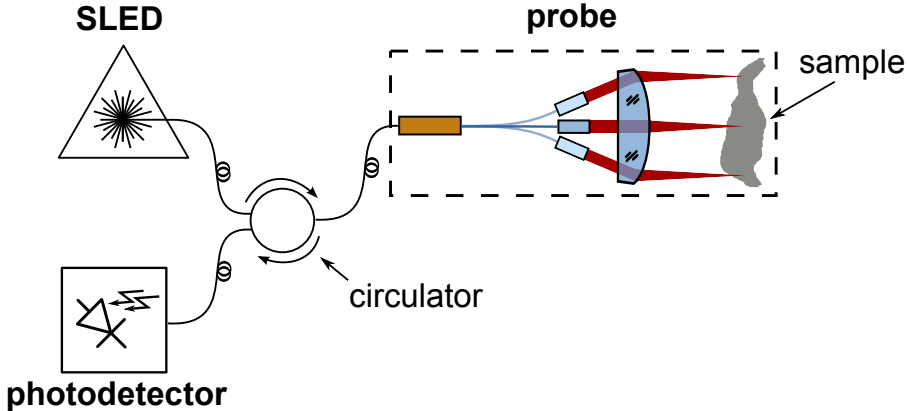


Figure 4.1: Setup used to measure the backreflectivity of the probe and for fiber-optical confocal microscopy. Light originating from the SLED is coupled to the probe through the circulator, while the backscattered light from the probe and sample is coupled to the photodetector.

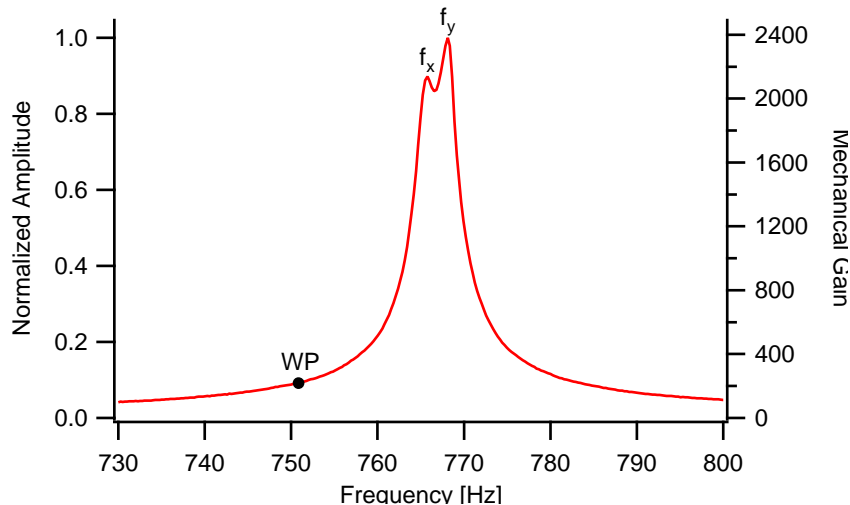


Figure 4.2: Dynamic behavior of the scanner in *Probe 2* under harmonic excitation. The two eigenfrequencies corresponding to the main axes of the scanner are marked as $f_x = 765.8 \text{ Hz}$ and $f_y = 768.1 \text{ Hz}$. For the imaging experiments, the scanner operates at a working point *WP* far away from the resonance, in order to minimize nonlinearities. The right axis shows the mechanical gain due to resonance, defined as the ratio of the displacement of the GRIN tip to the displacement of the piezoelectric tube tip.

each point of the spiral it is possible to reconstruct an image of the sample. This imaging technique is thus denominated fiber-optical confocal scanning microscope, a sub-type of LSM, whose theory of operation is described in ??.

4.3.1 Imaging

The setup used to measure the backreflectivity of the probe, shown in Figure 4.1, can be used directly for LSM. While the probe scans an object with a spiral pattern defined by the driving voltage datapoints $(\mathbf{u}_x[n], \mathbf{u}_y[n])$, the data acquisition system (DAQ) samples a stream of intensities at the photodetector $\mathbf{I}[n]$, as shown in Figure 4.3a. As these signals are generated and acquired synchronously, we expect that the intensity $\mathbf{I}[i]$ corresponds to a point in object space linearly related to the driving voltage of the piezoelectric scanner: $(x, y) = K_{\text{mech}}(\mathbf{u}_x[i], \mathbf{u}_y[i])$, where K_{mech} is a mechanical constant.

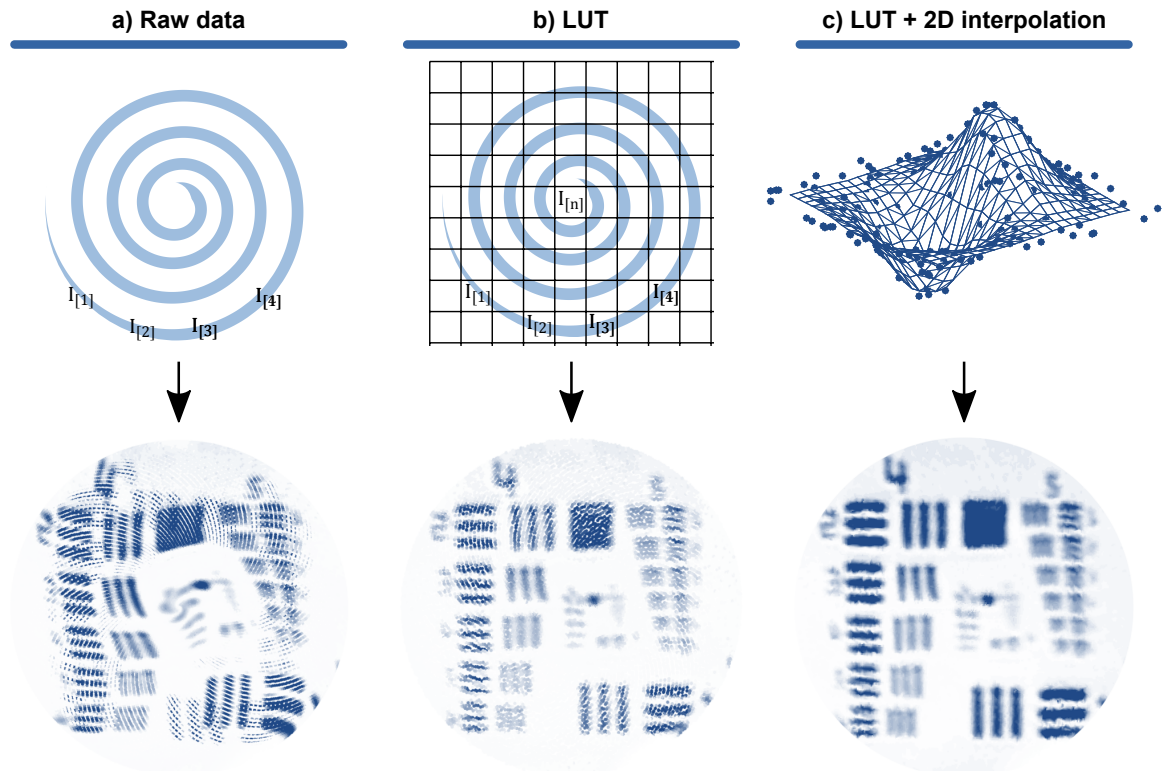


Figure 4.3: Different representations of the same acquired datapoints $\mathbf{I}[n]$ of a USAF 1951 resolution test chart. The full acquired spiral consists of 374 rings of 122 datapoints, adding up to 45500 datapoints measured at 91 kHz during 500 ms. The field of view is 1.1 mm.

a: Point cloud assuming ideal movement of the scanner. **b:** Point cloud after correcting the position of each dot using a lookup table. **c:** Raster image after performing a 2D interpolation from the data in d.

If all the datapoints $\mathbf{I}_{[n]}$ acquired during a full spiral are plotted as a color-coded dot located at the position $K_{\text{mech}}(\mathbf{u}_x[n], \mathbf{u}_y[n])$, the resultant image would look as in Figure 4.3a: distorted. Notice how the dot plot defines two overlaid swirled images. This proves that the previous assumption of linearity is not valid, and thus the relationship between $(\mathbf{u}_x[i], \mathbf{u}_y[i])$ and $(\mathbf{x}[i], \mathbf{y}[i])$ is neither linear nor simple. This

effect is caused by the subtle changes in the dynamic behavior of the fiber scanner at different oscillation amplitudes, and is typical of spiral fiber scanners [8]. There are two general methods to overcome this problem:

The first one involves closed loop operation, where the current position of the scanner is measured inside the probe and used by the plotting system to correct for the distortion [15].

The open loop alternative, used in this work, assumes that the distortion pattern is constant for a given driving signal. Then, the distorted spiral pattern ($x[i], y[i]$) can be measured after the assembly of the probe using a position sensitive device (PSD) and stored as a calibration lookup table. Once this calibration step is performed, any further frame is plotted by assigning a position ($\mathbf{x}[i], \mathbf{y}[i]$) to every measured intensity $I[n]$, as depicted in Figure 4.3b, resulting in a distortionless dot plot. This procedure can be performed in real time.

The dot plots which are obtained from spiral scanners have the inconvenient of non-uniform sampling, as can be seen in Figure 4.4. Thus, to ease the further processing of the acquired images, it is beneficial to convert the non-uniform dot plot into a cartesian raster image. This can be performed by 2D interpolation, resulting in Figure 4.3c.

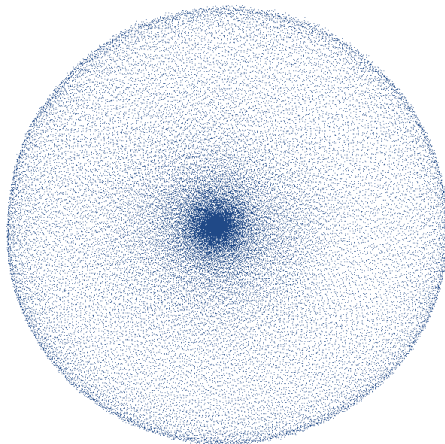


Figure 4.4: Sampling points of the scanner during a complete spiral cycle measured using a PSD. Notice the non-uniform sampling. Each one of the 45500 dots represents a sample point in object space. The coordinates of each point ($\mathbf{x}[i], \mathbf{y}[i]$) are used in a LUT to correct for the inherent sampling distortion characteristic of fiber scanners.

4.3.2 Lateral Resolution Measurement

The optical performance of the scanner is qualitatively evaluated by capturing a LSM image of a USAF 1951 resolution test chart with a spiral scanning pattern using the setup described in Figure 4.1. As can be seen in Figure 4.3c, element 4 of group 4 is resolved, indicating a resolution of 22 line pairs/mm or 45 μm .

4 Experimental Characterization

A more robust method for the calculation of the optical resolution is detailed in ???: by scanning the focus of the probe over a sharp chromium edge of the test chart, the edge spread function (ESF) shown in Figure 4.5a is obtained. By deriving and then performing a Fourier transform of the ESF, the MTF can be obtained, plotted in Figure 4.5b. Based on this curve the lateral resolution of the OCT beam path was determined at 21 line pairs/mm or 47.6 μm . A good concordance is observed

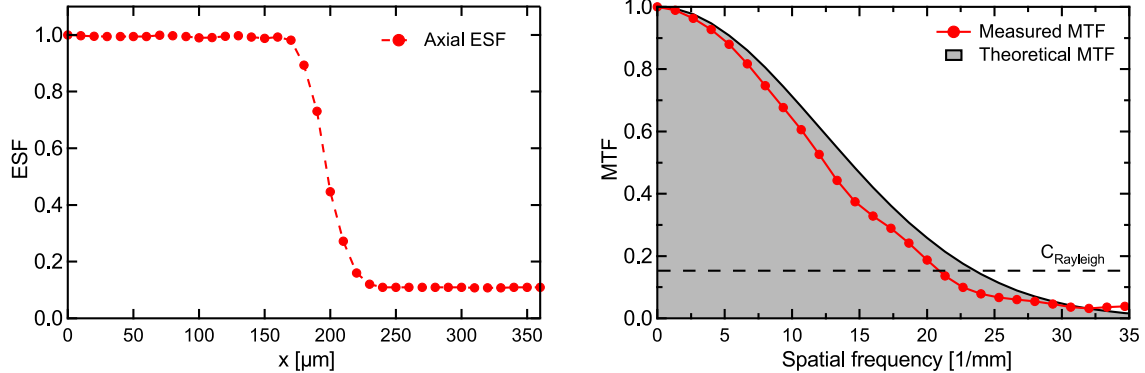


Figure 4.5: Left: Measured edge spread function (ESF) of the OCT beampath for the center of the field of view. Right: Corresponding MTF compared with the theoretical limit using the theory from ??.

between the shape of the analytical and the measured MTF curves of the scanning modality. However, the overall performance is reduced by 10% compared to the simulation. This deviation can be explained by small misalignments of the optical components induced by the process tolerances of the 3D-printed housing. Since a better alignment can be achieved in the silicon micro bench due to the higher precision of the MEMS processes a better match between simulation and reality can be expected for the multimodal probe.

4.3.3 Depth of Field Measurement

The depth of field (DoF) of the OCT imaging system can be determined by measuring how much light is backreflected upon a mirror while moving it through the z axis. The results from this experiment are plotted in Figure 4.6, where a full width half maximum (FWHM) DoF of 3.5 mm is calculated.

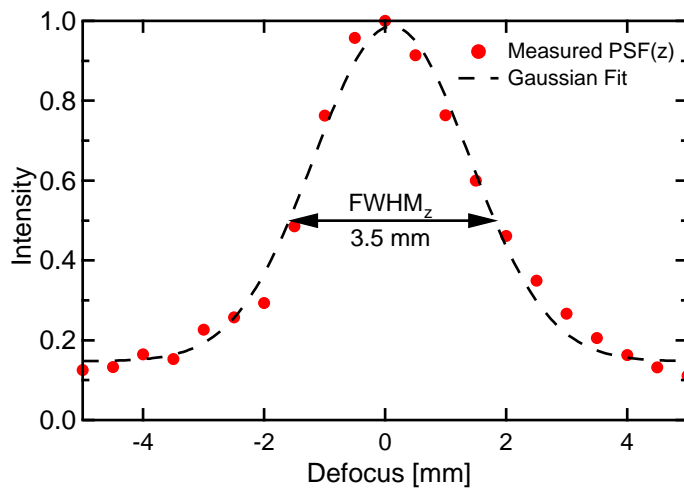


Figure 4.6: Measurement of the axial resolution of the single modality probe. The intensity of the light coupled back into the optical system after reflection on a mirror is plotted against the translation of the mirror by ± 4.5 mm from the focal plane of the probe.

4.4 OCT Imaging

The OCT characterization was performed using a swept-source OCT system of the Medical University Vienna. This system, represented in Figure 4.7 is operating with a center wavelength of $1.34\text{ }\mu\text{m}$, a bandwidth of 37 nm and a theoretical axial resolution in air of $26.9\text{ }\mu\text{m}$.

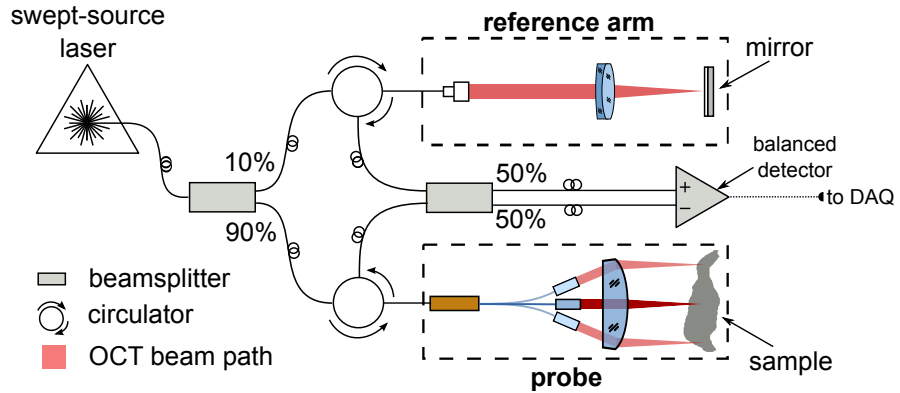


Figure 4.7: Medical University Vienna swept-source OCT system. Light originating from a swept-source laser is coupled to a balanced interferometer, where the optical path difference between the sample and the reference arm creates an interferogram which is converted to an electrical signal in a balanced detector.

The first OCT tests were performed as a proof of concept. Circular B-Scans of a colon polyp and a fingertip were captured with the single modality demonstrator, shown in Figure 4.8.

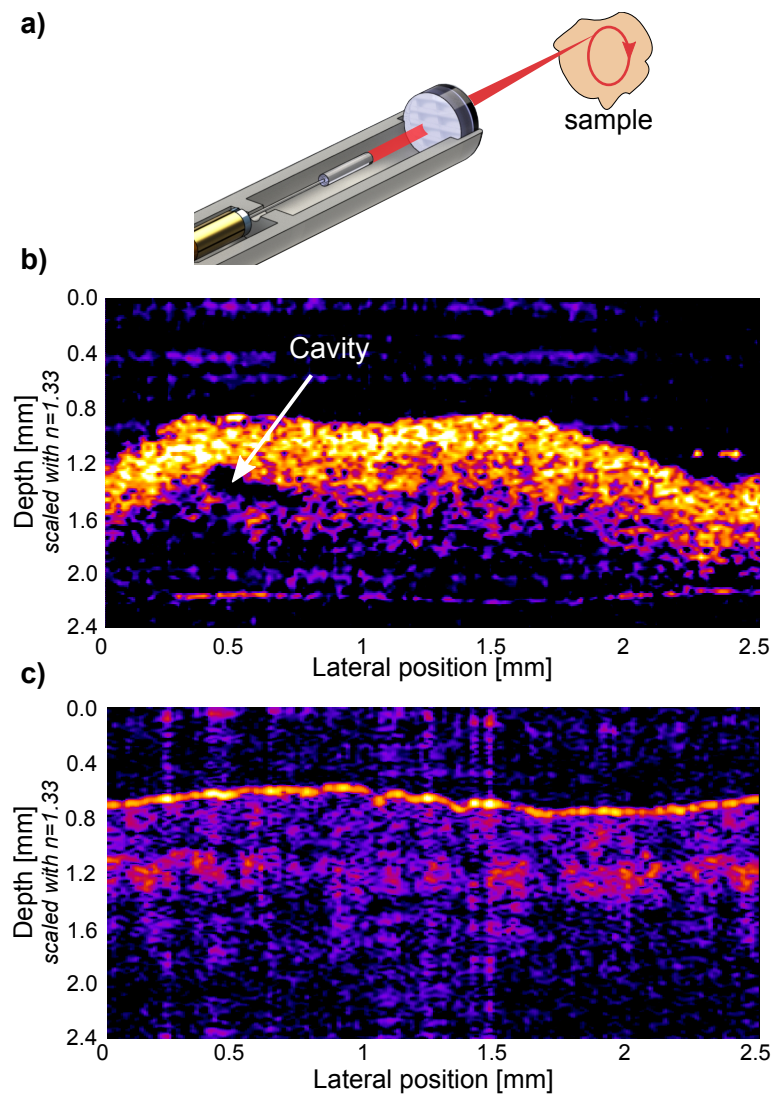


Figure 4.8: a) Illustration of the measurement arrangement for the circular B-Scan used as a proof of concept of OCT. b) Image of a circular OCT B-Scan of a colon polyp with a diameter $d = 0.8 \text{ mm}$. Structural changes within the tissue can be detected and at the current state of the investigation the images suggest that blood vessels can be detected. c) Image of a circular OCT B-Scan of a human finger tip.

4 Experimental Characterization

Bibliography

- [1] W. Drexler and J. G. Fujimoto, *Optical Coherence Tomography*. 2008.
- [2] S. Kretschmer, “Entwicklung einer bimodalen mikrooptischen Bank für endoskopische Anwendungen.”
- [3] G. D. Boreman and G. D. Boremann, *Modulation Transfer Function in Optical and Electro-Optical Systems*. 2001.
- [4] A. Arnau and D. Soares, “Fundamentals of piezoelectricity,” *Piezoelectric Transducers and Applications*, pp. 1–38, 2008.
- [5] C. J. Chen, “Electromechanical deflections of piezoelectric tubes with quartered electrodes,”
- [6] Marc J. Madou, *Fundamentals of Microfabrication: The Science of Miniaturization*. CRC Press, 2011.
- [7] H. D. Ford and R. P. Tatam, “Swept-source OCT with coherent imaging fibre bundles,” vol. 7503, no. 0, pp. 18–21, 2009.
- [8] E. J. Seibel, R. S. Johnston, and C. D. Melville, “A full-color scanning fiber endoscope,” *Optical Fibers and Sensors for Medical Diagnostics and Treatment Applications VI*, vol. 6083, pp. 608303–608303–8, 2006.
- [9] S. Moon, S.-W. Lee, M. Rubinstein, B. J. F. Wong, and Z. Chen, “Semi-resonant operation of a fiber-cantilever piezotube scanner for stable optical coherence tomography endoscope imaging.,” *Optics express*, vol. 18, no. 20, pp. 21183–21197, 2010.
- [10] D. Fertis, “Basic Theories and Principles of Nonlinear Beam Deformations,” *... and Methods to Solve Effectively Complex Nonlinear ...*, pp. 1–61, 2006.
- [11] C. M. Lee, C. J. Engelbrecht, T. D. Soper, F. Helmchen, and E. J. Seibel, “Scanning fiber endoscopy with highly flexible, 1 mm catheterscopes for wide-field, full-color imaging,” *Journal of Biophotonics*, vol. 3, no. 5-6, pp. 385–407, 2010.
- [12] T. Meinert, *3D-Scanner für konfokale Endomikroskopie*. PhD thesis, IMTEK, 2013.

Bibliography

- [13] L. Huo, J. Xi, Y. Wu, and X. Li, “Forward-viewing resonant fiber-optic scanning endoscope of appropriate scanning speed for 3D OCT imaging.,” *Optics express*, vol. 18, no. 14, pp. 14375–14384, 2010.
- [14] F. J. Rodríguez, D. Ceballos, M. Schüttler, A. Valero, E. Valderrama, T. Stieglitz, and X. Navarro, “Polyimide cuff electrodes for peripheral nerve stimulation,” *Journal of Neuroscience Methods*, vol. 98, no. 2, pp. 105–118, 2000.
- [15] I. L. Yeoh, P. G. Reinhall, M. C. Berg, and E. J. Seibel, “Self-Contained Image Recalibration in a Scanning Fiber Endoscope Using Piezoelectric Sensing,” *Journal of Medical Devices*, vol. 9, no. 1, p. 011004, 2014.